Diverging Behaviors of Simulated Tropical Cyclones in Moderate Vertical Wind Shear

CHAU-LAM YU,[a] BRIAN TANG,[a] AND ROBERT G. FOVELL[a]

[a] *Department of Atmospheric and Environmental Sciences, University at Albany, State University of New York, Albany, New York*

(Manuscript received 20 March 2023, in final form 27 September 2023, accepted 6 October 2023)

ABSTRACT: As a follow-on to a previous study that examined the tilt and precession evolution of tropical cyclones (TCs) in a critical shear regime, this study examines the processes leading to the subsequent divergent evolutions in tilt and intensity. The control experiment fails to resume its precession and reintensify, while the perturbed experiments with enhanced upper-level inner-core vorticity resume the precession after a precession hiatus period. In the control experiment, a mesoscale negative absolute vorticity region forms at the upper levels due to tilting in strong downtilt convection. This upper-level, negative-vorticity region is inertially unstable, causing the inward acceleration of upper-level radial inflow. This upper-level inflow subsequently becomes negatively buoyant due to diabatic cooling and descends, bringing midlevel, low equivalent potential temperature (θ_E) air into the inner-core TC boundary layer, significantly disrupting the low-level TC circulation. Consequently, the disrupted TC vortex in the control is unable to recover. The upper-level negative vorticity region is absent in the perturbed experiments due to weaker downtilt convection, preventing the emergence of the disruptive inner-core downdraft. The weaker downtilt convection is caused by several factors. First, a stronger circulation aloft advects hydrometeors farther downwind, resulting in greater separation of the cooling-driven downdraft from the convective updraft region, and thus weaker dynamically forced lifting at low levels. Second, the mean θ_E of the low-level air feeding downtilt convection is smaller. Third, there is stronger and deeper adiabatic descent uptilt, causing more low-θ_E air diluting the downtilt updraft region. These results show how the full vortex structure is important to diverging TC evolutions in moderately sheared environments.

KEYWORDS: Hurricanes/typhoons; Intensification; Mesoscale processes; Wind shear; Tropical cyclones

1. Introduction

The structure and intensity evolution of tropical cyclones (TCs) exhibit large variations in a moderately sheared environment (4.5–11.0 m s^{-1}; Rios-Berrios and Torn 2017). The complexity stems from the interactions of vertical wind shear (VWS) with a misaligned vortex, asymmetric rainband convection, precipitation-induced surface cold pools, surface enthalpy fluxes, among other factors (DeMaria and Kaplan 1994; Zhang and Tao 2013; Bhatia and Nolan 2013; Rios-Berrios et al. 2018). When embedded in a drier environment, the adverse impacts of VWS can cause further delay of intensification onset, or prevent intensification completely, due to the intrusion of dry, low equivalent potential temperature (θ_E) air from the environment, a process referred to as ventilation (Riemer et al. 2010; Tang and Emanuel 2010, 2012a,b; Alland et al. 2021a,b). Therefore, advancing our understanding of the combined effects of VWS with other pertinent environmental and internal TC factors is essential to further improve intensity forecasts (DeMaria et al. 2005; Bhatia and Nolan 2013; Finocchio and Majumdar 2017).

A TC vortex embedded in a vertically sheared environment may become misaligned due to the differential advection of its lower- and upper-level circulation centers, which results in enhanced low-level boundary layer convergence downshear and an asymmetric moisture distribution (Raymond 1992; Jones 1995, 2000; Frank and Ritchie 1999, 2001; Reasor et al. 2013; DeHart et al. 2014; Rios-Berrios and Torn 2017; Schecter 2022). Meanwhile, the balanced vortex response of the tilted vortex structure is associated with an asymmetric warm anomaly uptilt through adiabatic descent, which suppresses convection uptilt (Jones 1995; Chen et al. 2006; Boehm and Bell 2021). The combined effect is an asymmetric, wavenumber-1 pattern with enhanced rainband convection downtilt (Reasor et al. 2000; Corbosiero and Molinari 2002; Chen et al. 2006; Reasor and Eastin 2012; DeMaria 1996; Wang and Holland 1996; Frank and Ritchie 2001).

For sheared TCs, cyclonic precession of the vortex tilt vector toward the upshear quadrants has been frequently documented before the TC vortex becomes realigned and intensifies (Tao and Zhang 2014; Rios-Berrios et al. 2018). While early studies interpreted the vortex precession dynamics as linear (Reasor and Montgomery 2001; Schecter et al. 2002; Reasor et al. 2004; Reasor and Montgomery 2015) and nonlinear advection (Polvani 1991) of the upper- and low-level vorticity anomalies by the mean axisymmetric vortex, recent studies have found that the interaction between VWS, the misaligned vortex structure, and the asymmetric convection downtilt can result in a more complex vortex precession evolution. In examining the evolution of a tilted TC vortex in a shear-free environment, Schecter and Menelaou (2020) and Schecter (2022) found that midtropospheric vorticity generation by the strong asymmetric convection downtilt is essential to sustain a misaligned vortex structure, while nondivergent advection of coherent vorticity features can further cause nonmonotonic growth of the vortex tilt. Several other studies (Rios-Berrios et al. 2018; Nguyen and Molinari 2015; Chen et al. 2018), which examined the vortex tilt evolution of a sheared TC using full-physics simulations, suggested that the development of a deep subvortex near the downtilt-left precipitation centroid is important to the realignment process. The consensus among

Corresponding author: Chau-Lam Yu, cyu7@albany.edu

DOI: 10.1175/JAS-D-23-0048.1

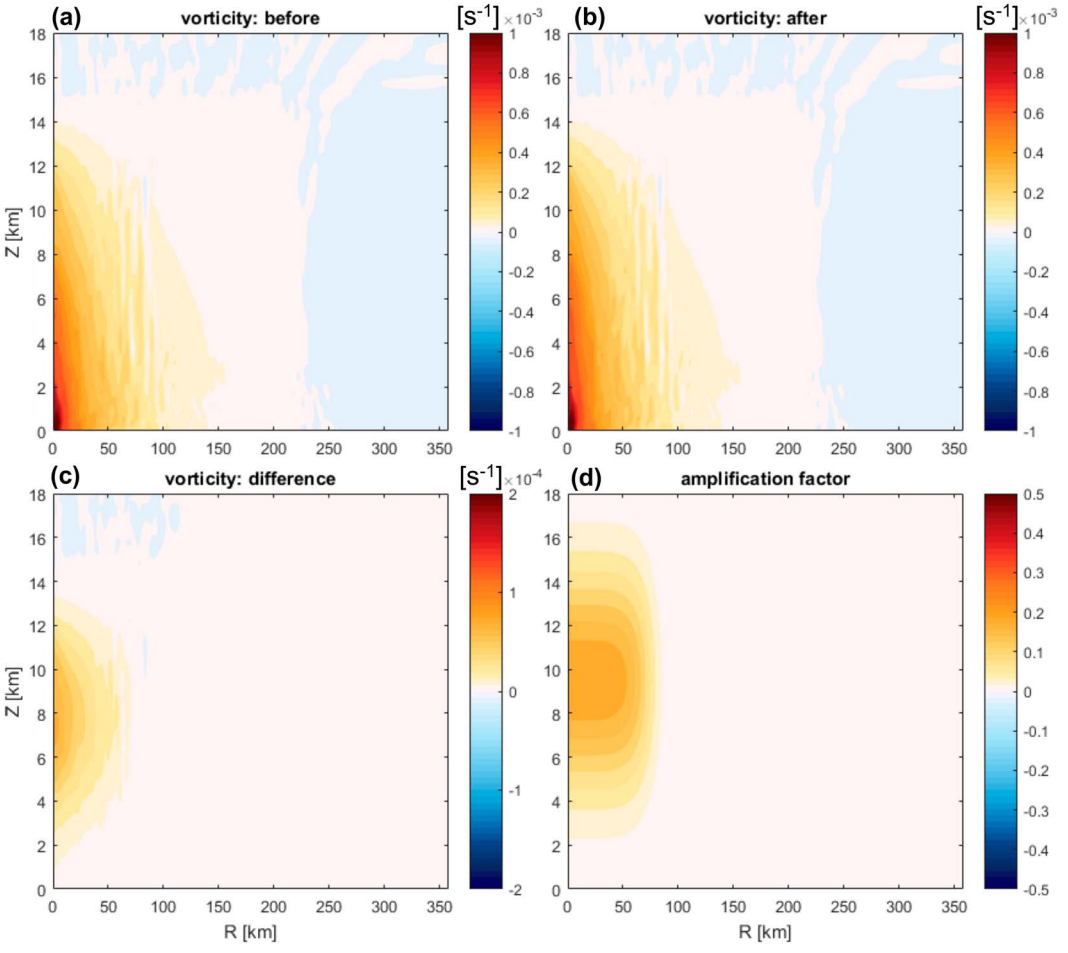

FIG. 1. Radius–height plot of the azimuthal mean vertical vorticity after the 12-h spinup period (a) before and (b) after a vorticity perturbation of $\alpha = 20$ is added, (c) the corresponding vorticity difference [(b) minus (a)], and (d) the amplification factor for $\alpha 20$. Reproduced from Yu et al. (2023).

these studies is that sustained vortex misalignment and the lack of intensification are linked to the asymmetric, persistent, downtilt convection that is lopsided relative to the low-level TC center (Rios-Berrios et al. 2018; Miyamoto and Nolan 2018; Alvey et al. 2020; Schecter and Menelaou 2020; Schecter 2020, 2022).

In addition to a misaligned vortex structure caused by VWS, TC development can be suppressed due to ventilation of low

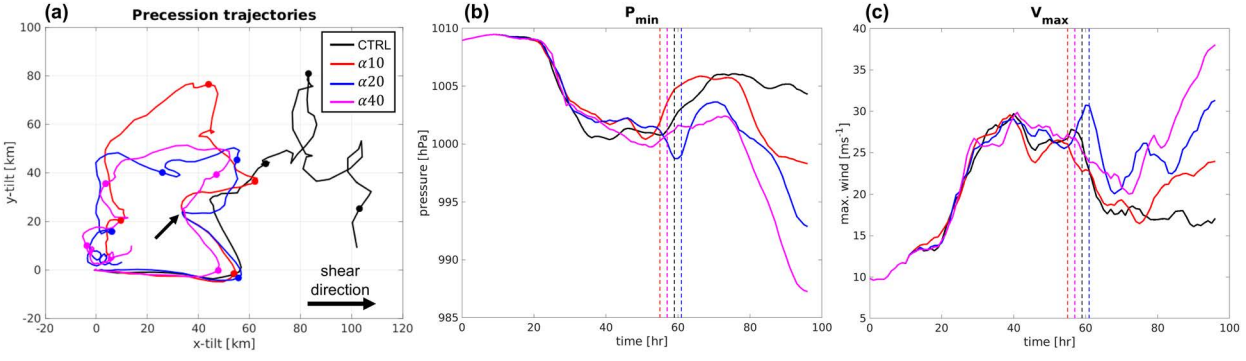

FIG. 2. (a) The vortex centroid tilt trajectories (6.5-km centroid relative to the 1.5-km centroid at the origin) of the simulations. Dots are every 24 h since the start of the simulations. The thin, black arrow indicates the emergence of the "kink" feature in the trajectories marking the precession hiatus. (b),(c) The time series of the minimum sea level pressure and maximum 10-m wind, respectively. Vertical dashed lines indicate the weakening start times t_w, which also correspond to the times when the inner-core downdraft reaches the surface.

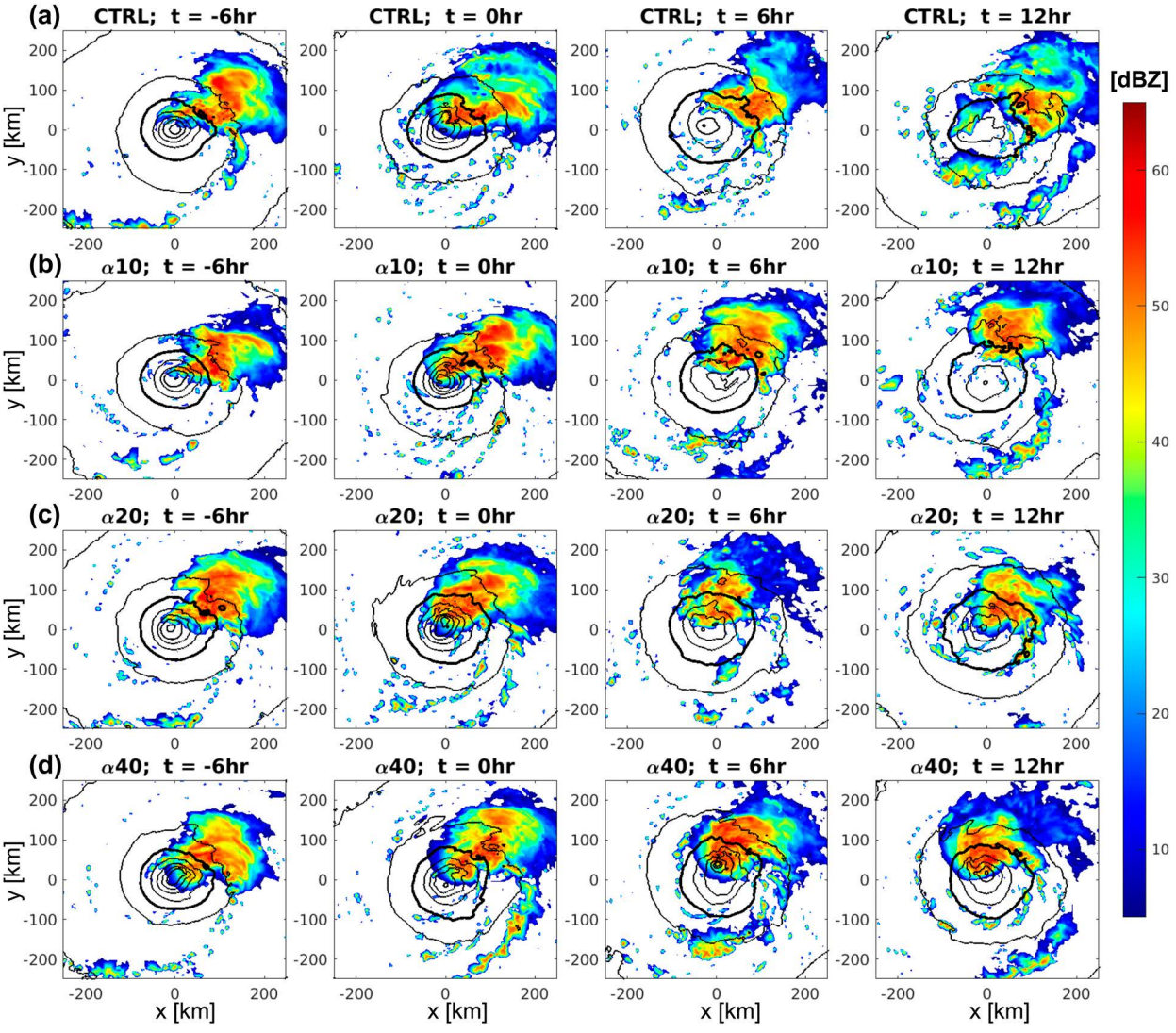

FIG. 3. Column-maximum reflectivity (shaded) and sea level pressure (contoured every 2 hPa and with a thick contour for 1010 hPa) at times (h) before and after the weakening start time for the (a) CTRL, (b) α10, (c) α20, and (d) α40 experiments.

equivalent potential temperature (θ_E) air from the environment (Riemer et al. 2010; Tang and Emanuel 2010, 2012a,b; Riemer and Laliberté 2015). Previous studies showed that there are two major ventilation pathways: a low-level, downdraft pathway and a midlevel, radial pathway. The downdraft pathway is associated with evaporatively driven downward flux of low-θ_E air into the subcloud layer in rainbands (Tang and Emanuel 2012a; Powell 1990; Hence and Houze 2008; Didlake and Houze 2009; Riemer et al. 2010, 2013; Alland et al. 2021a; Wadler et al. 2021), which could result in the suppression of inner-core convection and weakening of the TC if the θ_E deficit cannot be recovered through surface enthalpy fluxes before entering the inner-core region (Tang and Emanuel 2012b; Molinari et al. 2013; Riemer et al. 2013; Tao and Zhang 2014; Smith and Montgomery 2015; Gao et al. 2017; Chen et al. 2021; Alland and Davis 2022). Radial ventilation occurs when low-θ_E environmental air above the boundary layer intrudes into the inner core and dilutes the high-θ_E air. This effect can be enhanced in a sheared environment, where the greater storm-relative flow in the middle and upper levels of the storm enables greater radial penetration of low-θ_E air (Riemer and Montgomery 2011; Alland et al. 2021b; Fischer et al. 2023). Both downdraft and radial ventilation can weaken deep convection upshear, decrease the inner-core vertical mass flux, and inhibit intensification (Alland et al. 2021a,b).

The structural evolution of TCs in sheared environments also depends on the vertical structure of the TC vortex. Previous studies have shown that TCs with stronger upper-level vorticity have a stronger coupling between vertical layers, resulting in a greater ability of the TC to remain vertically coherent (i.e., have greater resiliency) in shear (Jones 1995; Reasor et al. 2004; Reasor and Montgomery 2015; Schecter et al. 2002; Schecter and Montgomery 2004; Schecter 2015). In

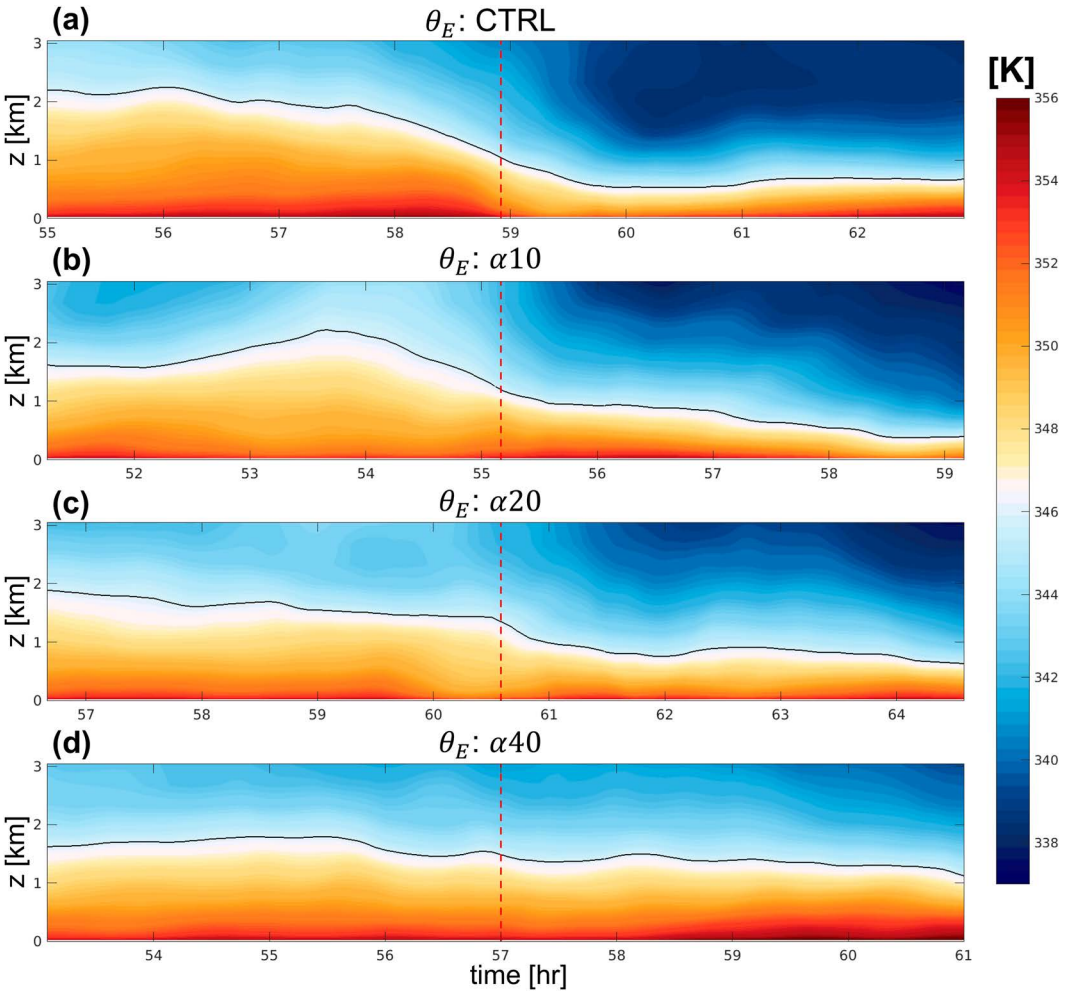

FIG. 4. Hovmöller diagrams of the averaged θ_E within 45 km of the center. Vertical red dashed lines show the time t_w in each simulation. The θ_E value of 346 K is contoured in black to highlight the decrease of θ_E in each experiment.

addition, a more robust upper-level circulation better protects the high-θ_E inner core from the storm-relative environmental wind (Riemer and Montgomery 2011; Alland et al. 2021b). Consequently, TC vortices with a greater initial depth tend to intensify more quickly (Peng and Fang 2021; Richardson et al. 2022; DesRosiers et al. 2023).

Using convection-permitting simulations of tropical cyclones in a sheared environment, Yu et al. (2023) examined the vortex tilt and precession evolution of an ensemble of TCs in the critical shear regime, which occurs when the VWS is sufficiently strong (7.5 m s^{-1} in these experiments) such that the TCs are nearly unable to overcome the inhibiting effects of VWS and intensify. Yu et al. (2023) explored the behavioral sensitivity of the TCs to the strength of the upper-level vortex by systematically enhancing the upper-level vorticity of the TCs at a restart point (12 h) in a control simulation. In this critical shear regime, all the members first exhibit a precession hiatus behavior, during which the cyclonic vortex precession pauses and the tilt magnitude increases. Near the end of the precession hiatus, the tilt and intensity evolutions of the members diverge, demonstrating substantial sensitivity to the mid- to upper-level vorticity structure. Focusing on the emergence mechanism of the precession hiatus, Yu et al. (2023) found that the midlevel vorticity generation at the downtilt rainband terminus region plays an important role in maintaining the quasi-stationary tilt configuration during the precession hiatus period. This midlevel vorticity generation is caused by the midlevel vortex stretching associated with the diabatic heating and cooling structure in the stratiform rainband region, indicating that the rainband diabatic processes modulated by the VWS are essential for hiatus maintenance.

As a follow-on study to Yu et al. (2023), we now focus on the divergence in the vortex tilt and intensity evolutions that occur just after the precession hiatus. The major questions addressed include the following: What are the processes and features that cause the divergent outcomes of the simulations? How do those features and processes contribute to the resumption of the vortex precession, or the lack thereof? What is the role of ventilation in causing the divergent outcomes of the simulations? The goal in

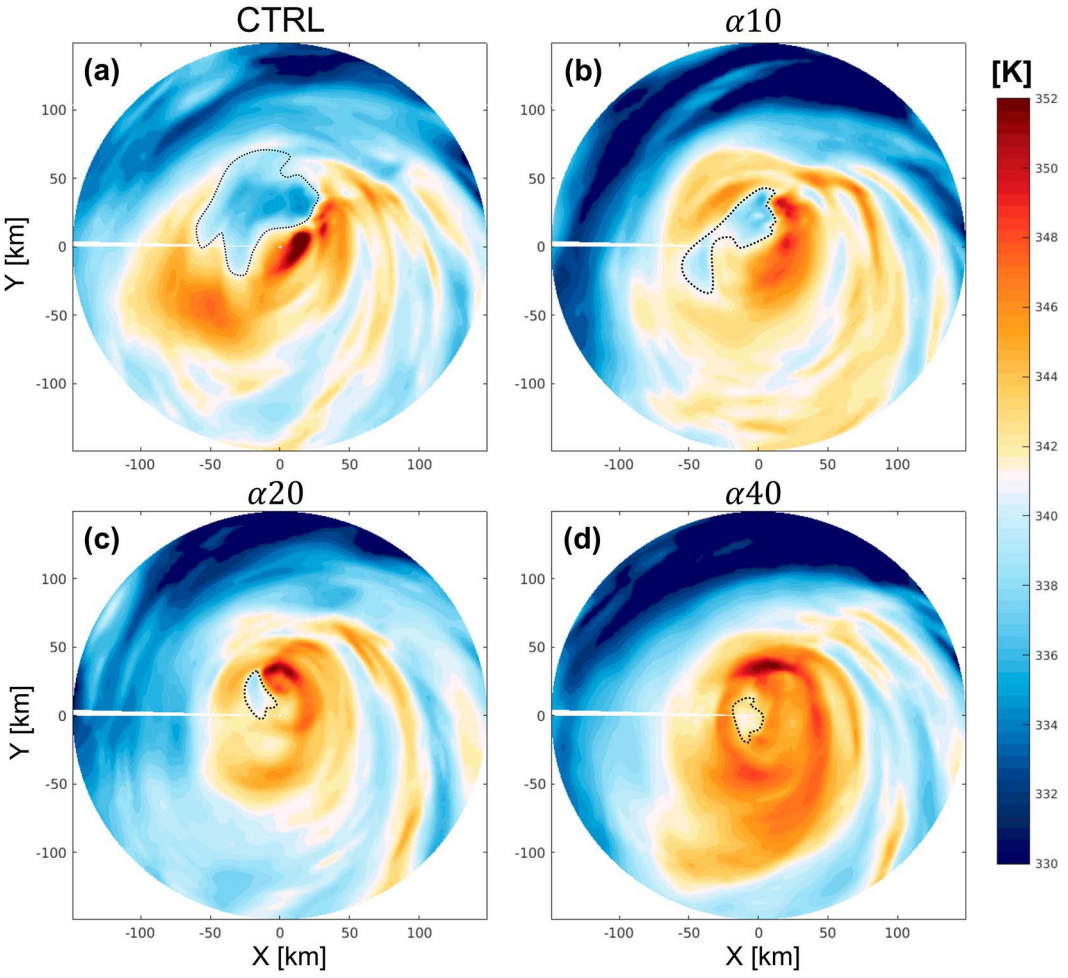

FIG. 5. The θ_E averaged between $z = 1$ and 2 km and over 1-h period after t_w. The black, dotted contour highlights the low-θ_E air intrusion of interest within the inner-core region.

addressing these questions is to advance our understanding of the sensitivity of intensity and structural evolutions near the critical shear regime.

The structure of this paper is as follows: Section 2 will introduce the details of the numerical simulations and measures of vortex tilt and precession and is followed by an overview of the divergent evolution of the simulations in section 3. Section 4 explores the mechanism of a key feature—a deep, inward intruding downdraft—that is central to the divergent evolution. Section 5 discusses a dynamical mechanism for the source of the downdraft air. Section 6 examines the downtilt convection strength and how its variability is related to the mid- to upper-level vortex strength. Section 7 concludes with the main findings of this study.

2. Methodology

a. Numerical model and experiment design

Idealized, convection-allowing simulations of tropical cyclones in a sheared environment are performed using the Cloud Model 1 (CM1; Bryan and Fritsch 2002), version 20.1. As described in Yu et al. (2023), the model simulations are performed on an f plane with a Coriolis parameter of 5×10^{-5} s^{-1} (20°N). The inner 728×728 km^2 region has uniform 2-km horizontal grid spacing, which is gradually increased from 2 to 16 km at the outer stretched portion of the domain. The total domain covers 1520×1520 km^2 and has periodic lateral boundary conditions. There are 59 vertical levels in total (model top set at 25 km), with variable spacing that gradually increases from 25 m at the surface to 500 m at heights $\geq$ 5500 m. The simulation is initialized with the analytic Rotunno and Emanuel (1987) vortex, with a maximum wind speed of 15 m s^{-1} at a radius of maximum wind of 82.5 km, and the wind radially decreases to 0 m s^{-1} at 412.5-km radius. The wind decreases linearly with height to 0 m s^{-1} at $z = 15$ km. The simulation is performed with a fixed sea surface temperature (SST) of 28°C. As in Yu et al. (2023) and Alland et al. (2021a), the initial relative humidity above 850 hPa is set to 50% throughout the entire domain. More details of the model configuration

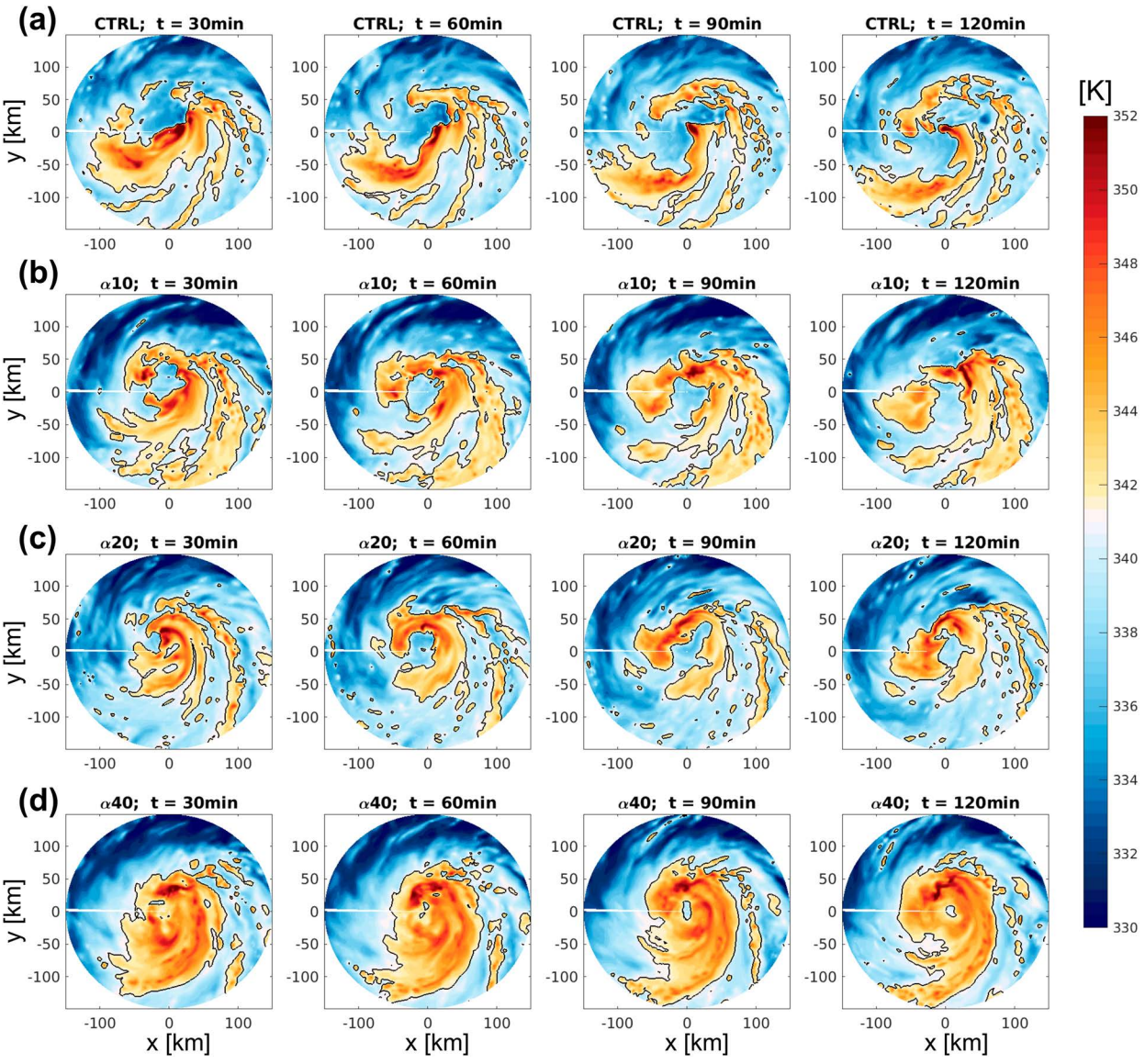

FIG. 6. The θ_E averaged between $z = 1$ and 2 km at times (min) after t_w for the (a) CTRL, (b) α10, (c) α20, and (d) α40 experiments. The θ_E value of 341.5 K is contoured to highlight the separation of the relatively high-θ_E inner-core air from the relatively low-θ_E downdraft air.

and parameterization schemes may be found in Yu et al. (2023).

A large-scale nudging method (Alland et al. 2021a), similar to the "time-varying point downscaling" technique of Onderlinde and Nolan (2017), is used to introduce VWS in all experiments. This large-scale nudging method nudges the domain-averaged horizontal wind to a prescribed wind profile (Alland et al. 2021a), rather than each individual grid point (Onderlinde and Nolan 2017). During the first 12 h, the simulations have no shear, after which VWS is added via a prescribed zonal background wind profile. The prescribed wind profile has -2 m s^{-1} zonal wind for $z < 1.5$ km and has a linear westerly shear of 7.5 m s^{-1} between $z = 1.5$ and 12 km, above which the prescribed wind is constant. The background wind reaches the prescribed profile approximately by 24 h and is then held constant thereafter.

As described in Yu et al. (2023), perturbation simulations are performed by adding an axisymmetric vorticity perturbation to the fields after the first 12-h spinup period. The vorticity enhancement is a Gaussian vertical profile that peaks at $z = 9.5$ km and has a standard deviation of 5 km, with an amplification percentage α. Figure 1 shows an example of the vorticity enhancement for $\alpha = 20$. Including the control experiment (CTRL), where $\alpha = 0$, a four-member set of experiments are run with $\alpha = 0$, 10, 20, and 40, labeled α10–α40, to examine the sensitivity of the vortex intensification

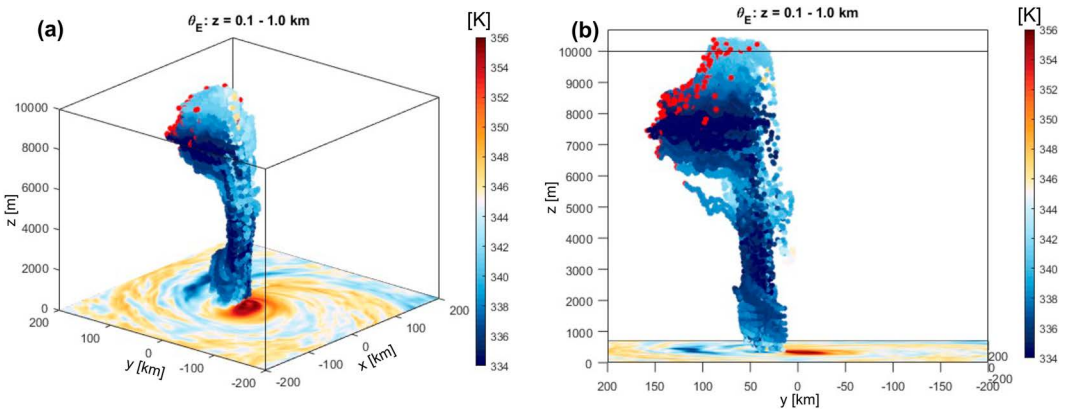

FIG. 7. Six-hour back trajectories for the CTRL experiment, initialized at grid points within the inner-core region where the θ_E is in the lowest quartile: (a) 3D view and (b) 2D view from the west to better visualize the parcel origin layer. The along-trajectory θ_E is colored in dots. The originating locations of the parcel trajectories are colored in red. Vertically averaged θ_E between $z = 0$ and 2 km is shown at the bottom.

and alignment process to the TC vorticity structure in the sheared environment.

b. *Measure of the TC vortex tilt*

As in Yu et al. (2023), the centroid-based methods discussed in Nguyen et al. (2014) and Ryglicki and Hart (2015) are used to determine the TC centers at a given level based on the vorticity field:

$$\mathbf{x}_{\text{center}} = \frac{\int_0^{2\pi}\int_0^R \zeta_z \mathbf{x}\, r\, dr\, d\lambda}{\int_0^{2\pi}\int_0^R \zeta_z r\, dr\, d\lambda}, \tag{1}$$

where $\mathbf{x}$ is the position vector, λ is the azimuthal angle, ζ_z is the relative vorticity, and R is the radius of integration, 120 km in this study. The tilt of the TC vortex is defined as the vector difference between the centers at $z = 6.5$ and 1.5 km.

3. Overview of model simulations

We now examine the tilt and intensity evolution of the simulations (Fig. 2). Once VWS is applied at 12 h, all experiments show a clear eastward tilt, which is then followed by a cyclonic precession after the tilt reaches about 50–60 km (Fig. 2a). As examined in Yu et al. (2023), a precession hiatus, which manifests as a pause in the cyclonic precession with a simultaneous increase in tilt magnitude, occurs in all simulations near 30 h when the tilt vector points northeast, resulting in a "kink" in the precession trajectory (thin arrow in Fig. 2a). The precession hiatus lasts about 25 h (from 30 to 55 h), during which the intensity of all experiments remains fairly steady (Figs. 2b,c).

All of the experiments exhibit weakening between 55 and 70 h (Figs. 2b,c). We define the start time of the weakening period as t_w, based on a sustained decrease in the maximum 10-m wind ($v_{\max}$) lasting at least 6 h by at least 6 m s^{-1}, and we will refer to t_w in later analyses. This period is also when the simulations diverge in the vortex tilt evolution. The CTRL simulation weakens the most, with an increase of minimum sea level pressure of about 5 hPa and a decrease of maximum wind speed of about 10 m s^{-1}. The CTRL simulation also distinctly fails to resume precession, and the vortex tilt continues to generally increase. The α10 simulation weakens to a similar degree as the CTRL simulation, and the vortex tilt increases toward the north through 72 h. Thereafter, the TC precesses cyclonically, the tilt magnitude decreases, and reintensification occurs after 72 h. In contrast, there is less weakening in the α20 and α40 simulations, and both restart the cyclonic precession, tilt reduction, and intensification more quickly.

To assess the structural changes during the period when the simulations diverge, Fig. 3 shows the column-maximum reflectivity and sea level pressure from 6 h before to 12 h after the weakening start times. About 6 h before their weakening, all members have similar intensity and downshear-left reflectivity maxima. At 6 h after the weakening commences, the minimum sea level pressure in all members increases. Importantly, at 12 h, the area of largest reflectivity in the CTRL simulation is still located in the downshear-left quadrant, and relatively far from the center, while the area of largest reflectivity in the α experiments has propagated cyclonically toward the upshear quadrants, particularly in the α40 experiment. Additionally, the convection is closer to the center in the α20 and α40 experiments.

Why do all the storms tend to weaken around 55–70 h? Figure 4 shows that the azimuthally averaged, low-level, inner-core θ_E in all of the experiments has a substantial drop around t_w (vertical red dashed lines in Fig. 4). The decrease in θ_E in the CTRL simulation is more pronounced and deeper, as indicated by the lowering of the 346-K moist isentrope (black contour in Fig. 4a). On the other hand, the θ_E decrease in the α10 simulation is slightly smaller, especially near the surface (Fig. 4b). The θ_E decrease in the α20 simulation is smaller still (Fig. 4c), and the decrease is barely noticeable in the α40 simulation (Fig. 4d).

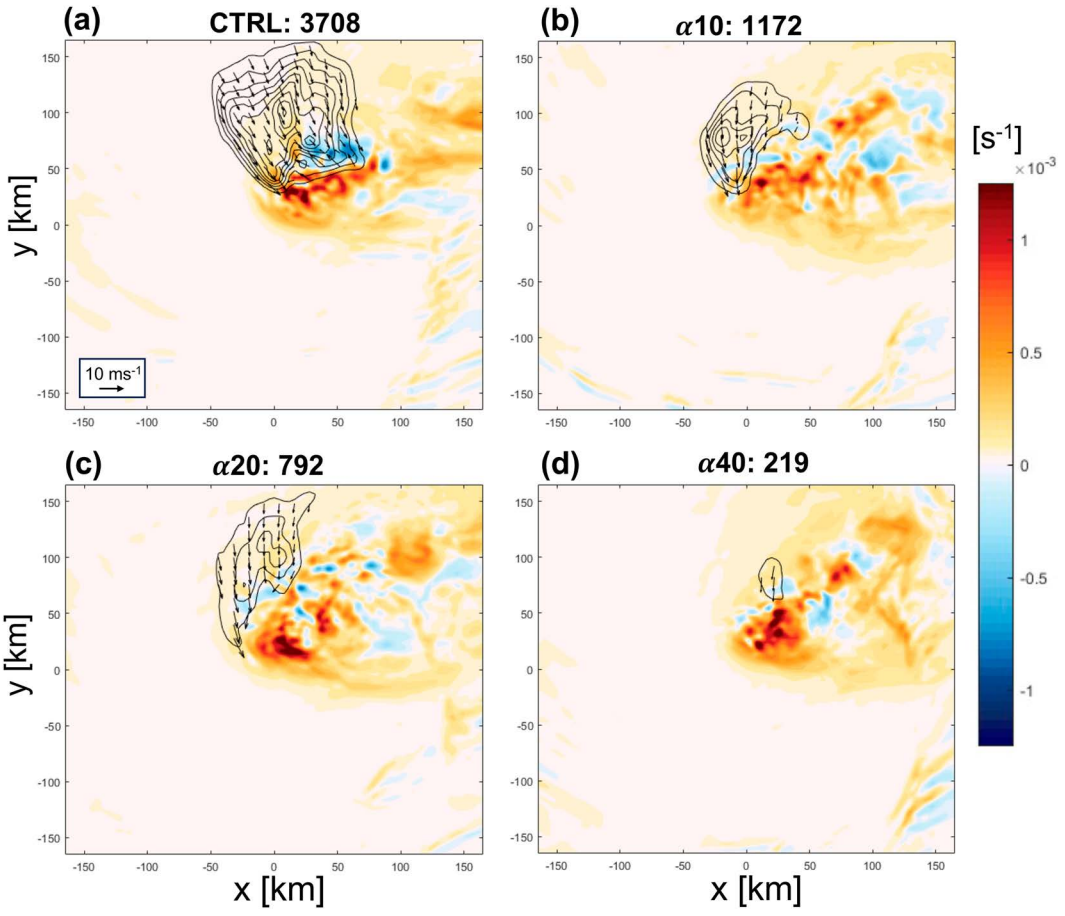

FIG. 8. Vertically averaged absolute vorticity between $z = 7$ and 10 km for the (a) CTRL, (b) α10, (c) α20, and (d) α40 simulations. The black contours show the normalized trajectory density within the 7–10-km layer, contoured every 0.1. The trajectory density is normalized by the total number of trajectories in the CTRL simulation. The total number of trajectories of each experiment is given in each panel title. Horizontal wind vectors within the trajectory region are shown by the black arrows.

Examining the spatial structure of the low-θ_E intrusion more closely (Fig. 5), a patch of low-θ_E air emerges northwest or west of the center (indicated by the black, dotted contour in Fig. 5) in all the experiments. In the CTRL simulation, this inward intruding low-θ_E air is colder and more widespread. Subsequently, this air results in strong disruption to the high-θ_E core (Fig. 6a) and low-level circulation, stunting the storm intensity. This disruption explains why t_w (determined based on a sustained weakening of v_{max}) corresponds well with the drop of boundary layer θ_E, as shown in Fig. 4. The low-level circulation in the CTRL simulation does not reorganize and reintensify after the disruption, at least over the duration of the simulation. The intruding low-θ_E air in the α10 simulation is also disruptive to the high-θ_E core, but the low-θ_E air does not flood the inner core as severely as in the CTRL simulation (Fig. 6b). In the rest of the α experiments, the inner-core low-θ_E air intrusion is weaker and smaller, causing less disruption to the high-θ_E inner core (Figs. 6c,d). In general, the larger the α, the weaker the intruding low-θ_E air, which allows for quicker recovery of the TC inner-core structure.

4. Analysis of the inner-core downdraft

a. *Back-trajectory analysis*

Given that all the members experience weakening of various degrees and show intruding low-θ_E air, where does the inner-core low-θ_E air originate from, and why is the intruding low-θ_E air in the CTRL simulation more prominent than the other α experiments?

To address these questions, we use the Lagrangian Analysis Tool (LAGRANTO; Wernli and Davies 1997; Sprenger and Wernli 2015) to examine the backward trajectories of the inner-core low-θ_E air to investigate its origin and structure. The initial locations of the back trajectories are seeded at levels below $z = 2$ km and at grid points within 48 km of the center that have a θ_E less than the 25th percentile for that layer. The number of trajectories for the four experiments is 3708 (CTRL), 1172 (α10), 792 (α20), and 219 (α40), which is proportional to the degree of low-θ_E intrusion in the inner core. Backward trajectories are integrated for 6 h. As an example, Fig. 7 shows back trajectories for the CTRL experiment. The

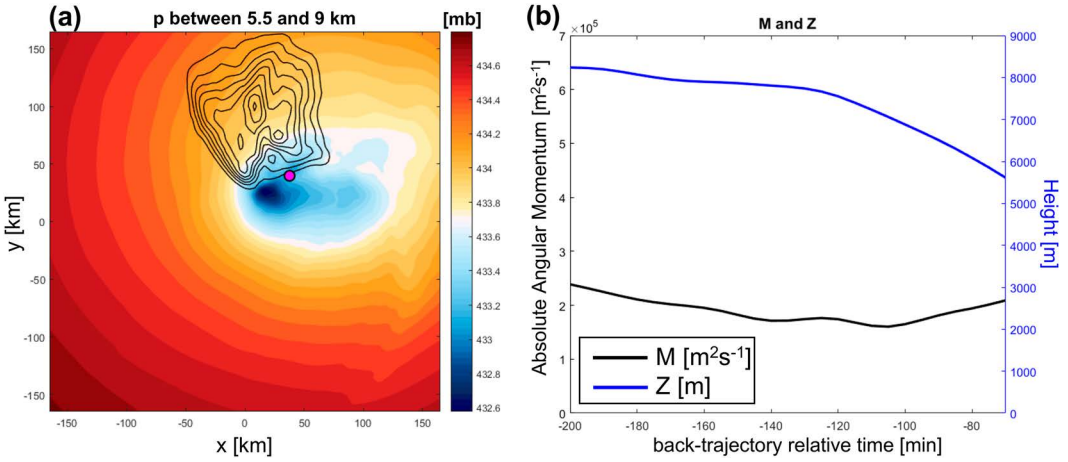

FIG. 9. (a) Vertically averaged pressure between $z = 5.5$ and 9 km (shading) and normalized trajectory density in the 7–10-km layer (contours every 0.1) for the CTRL simulation. The magenta dot indicates the optimal center (see text). (b) Time series of the average absolute angular momentum M (black), defined with respect to the optimal center, and height Z (blue) of the trajectories.

low-θ_E air mostly originates between 6- and 10-km height (Fig. 7), advecting radially inward above 6 km and then descending rather steeply, which brings low-θ_E air from the mid- to upper troposphere directly into the inner core. Back trajectories in the other experiments share the same descending pattern with similar originating θ_E values (about 340 K). It is, therefore, the amount of intruding low-θ_E air that determines the degree of disruption to the TC.

To explore the dynamics of the mid- to upper-tropospheric origin of the descending low-θ_E air, we examined the absolute vorticity structure between 7- and 10-km height across the experiments (Fig. 8), together with the trajectory density within this layer. While positive upper-level vorticity in all of the experiments is displaced toward the downshear-left quadrant, consistent with the tilt direction, the CTRL experiment develops a more organized positive–negative dipole in absolute vorticity and the transition zone between the positive and negative vorticity delineates the southern edge of the trajectory density field. In contrast, increasing α results in fewer trajectories. In addition, the areas of negative vorticity in the α experiments are more scattered compared to those in the CTRL simulation. We will show in the next section that there is a connection between the negative absolute vorticity structure and trajectory behavior.

b. *Dynamical relevance of the negative absolute vorticity region*

We now focus on the CTRL experiment to examine the physical connection between the inflow of low-θ_E air and the negative absolute vorticity region to understand the mechanism contributing to the source of the downdraft air. To do so, we generalize a framework used to diagnose inertial instability.

OPTIMAL PRESSURE CENTROID BASED ON ABSOLUTE ANGULAR MOMENTUM CONSERVATION

In an axisymmetric flow, negative absolute vorticity is a necessary and sufficient condition for inertial instability (Ooyama 1966). However, for a tilted TC vortex in shear, the pressure field at each level is asymmetric, and the pressure minimum at each level is displaced downtilt relative to the surface pressure minimum. An issue associated with this asymmetric pressure structure is that the absolute angular momentum (M) of the air parcels may not be conserved due to a nonzero pressure gradient torque (PGT) associated with the asymmetric pressure field. In addition, the amount of PGT is also sensitive to the choice of the center location with respect to which the angular momentum is defined. These two obstacles preclude a direct application of the classic inertial instability framework in our present case.

However, by defining an "optimal" center for a set of inflow air parcels of interest, we will show that the dynamics of the inward acceleration of parcels at the upper-level source of the downdraft resembles that of classic inertial instability, despite the inherent asymmetry in the tilted vortex.

The storm-relative absolute angular momentum conservation with respect to a given center may be derived from Eq. (A7) of Yu et al. (2021):

$$\frac{DM}{Dt} = -\frac{1}{\rho}\frac{\partial p}{\partial \lambda} + rF_{\lambda} - rfu_c - r\frac{\partial v_c}{\partial t}, \tag{2}$$

where D/Dt is the Lagrangian derivative, $\partial/\partial t$ is the Eulerian time derivative following the storm, r is the radius, $M = rv + (1/2)fr^2$ is the storm-relative absolute angular momentum with f being the Coriolis parameter and v being the tangential wind relative to the given center, λ is the azimuthal angle, F_{λ} is the tangential component of momentum forcing, and u_c and v_c are the radial and tangential wind components due to the storm translation. The terms on the right-hand side of (2) are the PGT, frictional torque, motion-induced radial flux of planetary vorticity, and effects of storm-translation acceleration. Above the boundary layer, the last three terms on

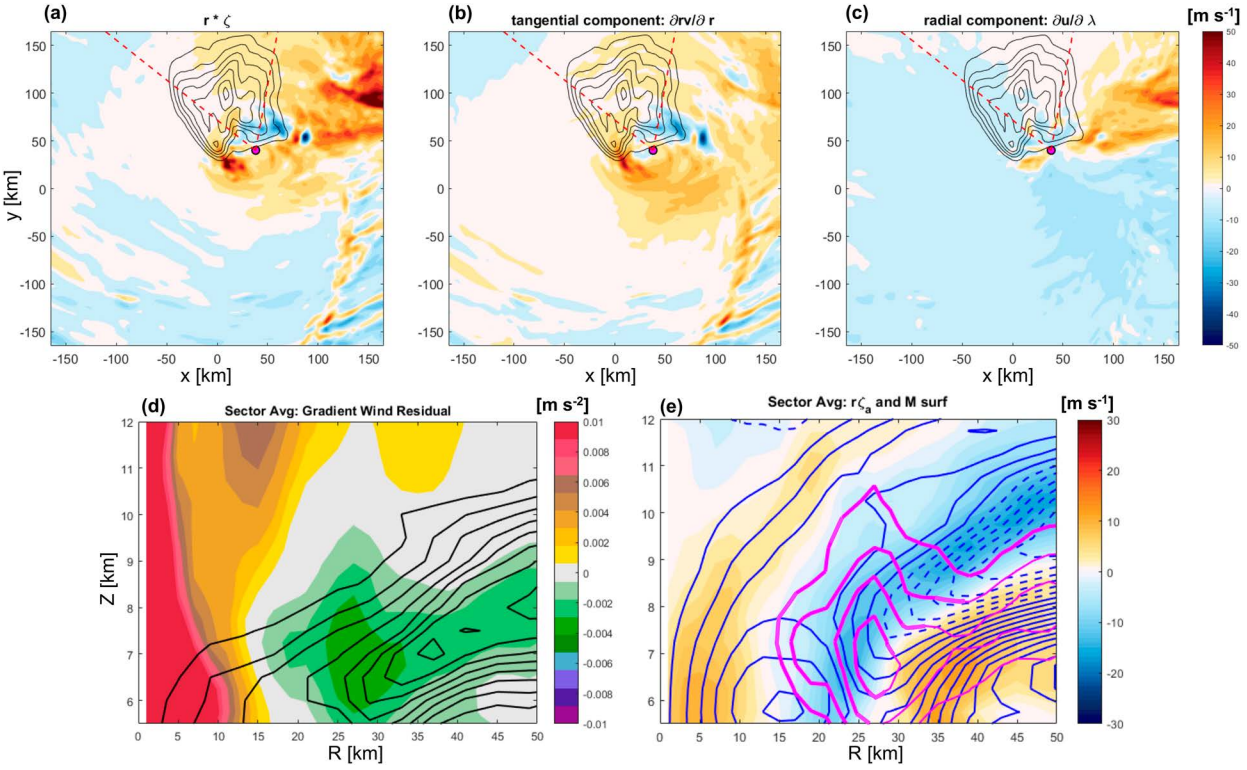

FIG. 10. Plan view of (a) radius times relative vorticity averaged between $z = 5.5$ and 9 km (shaded) and normalized trajectory density in the 7–10-km layer (contours every 0.1) for the CTRL simulation. The two red dashed lines demarcate the sector of interest. (b),(c) The tangential and radial components of the radius-weighted relative vorticity, respectively. (d) The azimuthally averaged sector gradient wind residual (shaded) and the trajectory density (contours every 0.1). (e) The azimuthally averaged sector tangential component of the absolute vorticity (shaded) and the absolute angular momentum with respect to the optimal center (contours every 2×10^4 m^2 s^{-1}). The gradient wind residual is contoured in magenta at 0, −0.001, −0.002, and −0.003 m s^{-2}, with the region overlapping negative vorticity given by thicker contours.

the right-hand side of (2) are significantly smaller than the first term. The objective is to seek an "optimal" center where the angular momentum defined with respect to this center would be maximally conserved along the trajectories. In other words, assuming inviscid flow ($F_\lambda = 0$) and negligible effects due to storm translation, this is equivalent to minimizing the PGT with respect to the optimal center along the trajectories. The minimization procedure is elaborated upon in appendix A. The result of the minimization yields an optimal center (magenta dot in Fig. 9a) at the southern edge of the trajectory density field. Figure 9b shows that the average along-trajectory M has a Lagrangian tendency of −10 m^2 s^{-2} from $t = -200$ to −100 min (back-trajectory time). This tendency, caused by PGT in (2), is one order of magnitude smaller than advection tendency (~100 m^2 s^{-2}, not shown), demonstrating that this choice of optimal center serves to approximately conserve M along this set of inflow trajectories.

Defining the radius and the wind velocity relative to the optimal center, and focusing only on the trajectory area, the radius-weighted relative vorticity (Fig. 10a) is dominated by the tangential component ($\partial rv/\partial r$; Fig. 10b), and the radial component ($\partial u/\partial \lambda$) has a smaller contribution (Fig. 10c). Thus, the absolute vorticity can be approximated as

$$\zeta_a \approx \frac{1}{r}\frac{\partial rv}{\partial r} + f = \frac{1}{r}\frac{\partial\left(rv + \frac{1}{2}fr^2\right)}{\partial r} = \frac{1}{r}\frac{\partial M}{\partial r}. \tag{3}$$

Meanwhile, since M is approximately conserved along the trajectories,

$$\frac{\partial M}{\partial t} + u\frac{\partial M}{\partial r} + \frac{v}{r}\frac{\partial M}{\partial \lambda} + w\frac{\partial M}{\partial z} \approx 0. \tag{4}$$

In addition, the radial advection of M dominates $[w(\partial M/\partial z) \sim (v/r)(\partial M/\partial \lambda) \ll u(\partial M/\partial r)]$ (not shown). Importantly, the upper-level negative ζ_a region is collocated with radial inflow, which is largely irrotational. This implies a negative radial advection of M in the negative vorticity region, i.e., $-u(\partial M/\partial r) \approx -ru\zeta_a < 0$ (since u and ζ_a are both negative). In other words, smaller M is advected toward the optimal center, making the wind more subgradient and driving an acceleration inward toward the optimal center.

To further quantify and visualize this effect, we define a sector encompassing the bulk of the trajectories and emanating from

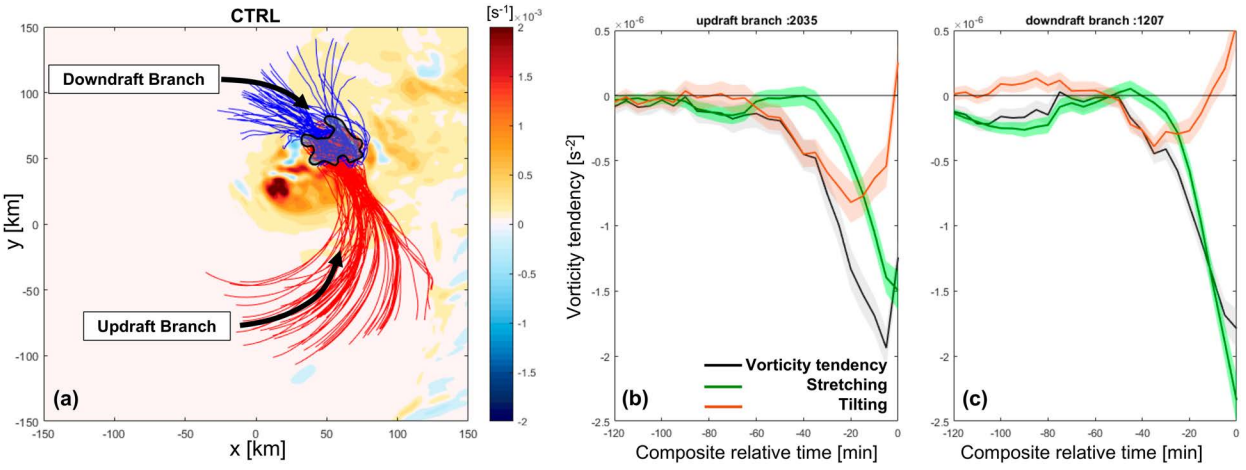

FIG. 11. (a) Absolute vorticity averaged between $z = 5.5$ and 9 km for the CTRL simulation, together with back trajectories initialized at the negative vorticity region. The red trajectories comprise the updraft branch, and the blue trajectories comprise the downdraft branch. The black contour shows negative vorticity of -5×10^{-5} s^{-1}. (b) Time series of the mean absolute vorticity tendency along the trajectories (black), together with the stretching (green) and tilting (brown) contributions for the updraft branch trajectories. The shaded regions show ±1 standard deviation. (c) As in (b), but for the downdraft branch.

the optimal center (red, dashed lines in Fig. 10a). Figure 10d shows the inflow trajectories are mostly subgradient (negative gradient wind residual), indicating that the radial inflow is accelerating toward the optimal center. In addition, a large portion of the subgradient region overlaps with the negative absolute vorticity region (Fig. 10e), indicating that the inward advection of M in this overlapping region increases the subgradient imbalance, further accelerating the inflow. The feedback process between radial inflow and subgradient force described here is consistent with the dynamics of classic inertial instability. Therefore, the negative vorticity region plays an important dynamical role in drawing in low-θ_E air that feeds the strong inner-core downdraft ventilation. In contrast, the lack of an organized negative vorticity region in the α experiments implies a more inertially stable vortex structure and less ability for low-θ_E inflow to feed inner-core downdraft ventilation.

5. Negative vorticity generation

We now explore how the negative vorticity region is generated, and why it is more organized in the CTRL simulation, but not in the other α experiments.

Source of negative vorticity

To identify the source of the negative vorticity region, we performed a back-trajectory analysis from the core of the negative vorticity region in the CTRL simulation. We seeded parcel trajectories at grid points where the absolute vorticity was less than -5×10^{-5} s^{-1} between $z = 7$ and 10 km from -2 to -1 h before t_w in 5-min increments. A subset of the back trajectories and initialization region (black contour) are shown in Fig. 11a, which reveals that two airstreams pass through the negative vorticity region. One branch of air originates northwest of the negative vorticity region at upper levels (near 7–10 km, blue trajectories in Fig. 11a), which is part of the inward flow of air toward the optimal center that we showed previously. This branch of air approximately accounts for 35% of the total trajectories. The rest (65%) of the trajectories originate from the cyclonic upwind side of the negative vorticity region and are characterized by strong upward motion before entering the negative vorticity region (red trajectories in Fig. 11a).

An absolute vorticity budget is calculated along the trajectories (Figs. 11b,c):

$$\frac{D\zeta_a}{Dt} = \boldsymbol{\zeta}_h \cdot \nabla_h w - \zeta_a \delta + \nabla_h \times \mathbf{F}, \tag{5}$$

where $\boldsymbol{\zeta}_h$ is the horizontal vorticity vector, δ is the horizontal divergence, and $\mathbf{F}$ is the momentum forcing. The terms on the right-hand side are tilting, stretching, and the vorticity source due to momentum forcing, which we ignore because it is small in the free troposphere. Both the updraft and downdraft streams have a strong negative vorticity tendency after -50 min. The separation between tilting and vortex stretching terms indicates that negative vorticity is first generated through tilting of horizontal vorticity by differential vertical velocity, i.e., $\boldsymbol{\zeta}_h \cdot \nabla_h w$. The negative vorticity is subsequently enhanced by stretching.

6. Downtilt convective updraft strength

Given the important role of tilting in generating the midtropospheric negative vorticity, we now examine the relationship between the downtilt convective updraft strength and the tilting magnitude across the experiments.

As shown in Fig. 12, the column-integrated vertical mass flux in the downtilt convective rainband is strongest in the CTRL simulation (Fig. 12a) compared to that in the α experiments (Figs. 12b–d). In contrast, the upward mass flux field of the α experiments is less intense. To show how the differences in the downtilt convective updraft strength impact the tilting

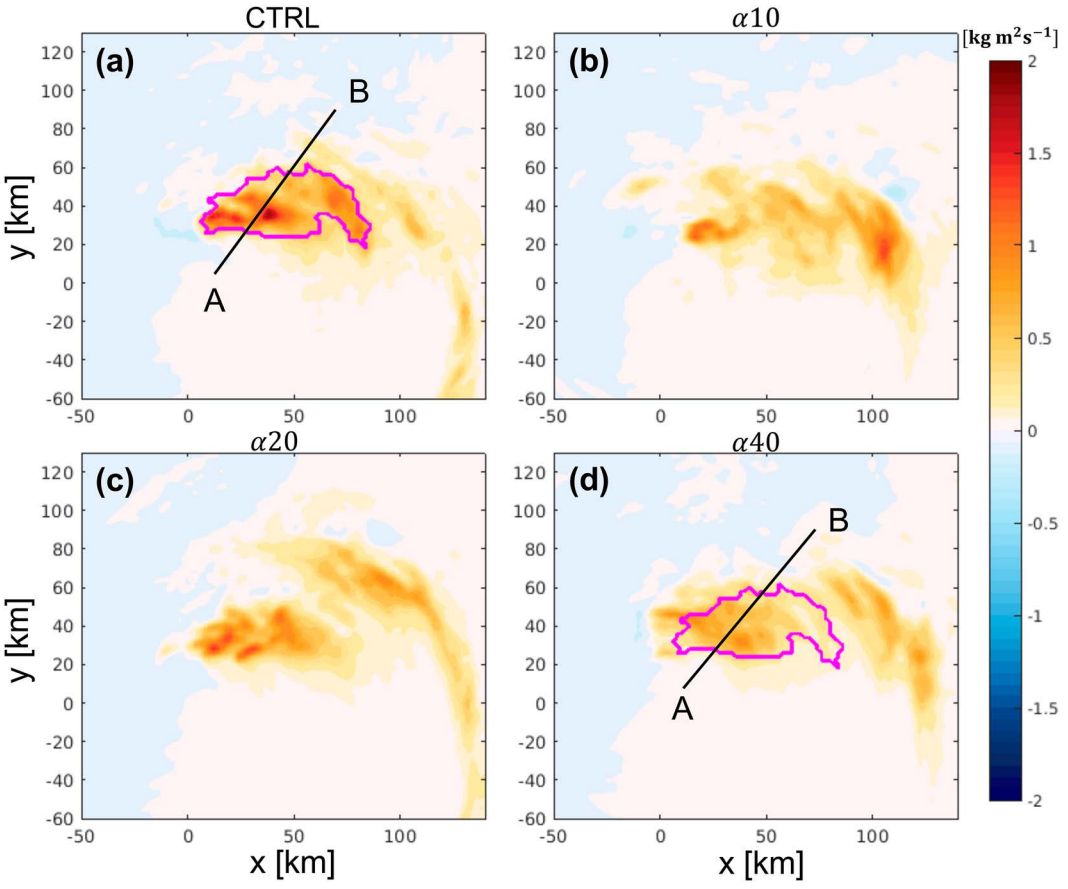

FIG. 12. The vertically integrated vertical mass flux between $z = 1$ and 10 km, averaged from -4 to -2 h before t_w for the (a) CTRL, (b) α10, (c) α20, and (d) α40 simulations. The origin in each panel is the location of the TC center at 1.5-km altitude. The magenta contour in (a) and (d) indicates the seeding regions for back-trajectory calculations (see text). Cross sections (A–B; see Fig. 15) for the CTRL and α40 simulations are indicated by the two black, solid lines.

magnitude, Fig. 13 shows histograms of the vertical velocity over the downtilt convection region where the mean tilting between 8 and 12 km is less than -2.5×10^{-3} s^{-1} h^{-1} from -4 to -2 h before t_w. Within the negative tilting region, the CTRL simulation has the broadest updraft distribution, with a substantial portion of the distribution exceeding 4 m s^{-1}. The α10 experiment has a distribution that peaks around 2 m s^{-1} but quickly drops beyond 3 m s^{-1}. The distributions for α20 and α40 have the bulk of their distributions between -2 and 2 m s^{-1}. The differences in downtilt convective updraft strength impose a strong impact on $\nabla_h w$ and, thus, the tilting magnitude, and reasons for these updraft differences will be examined next. Differences in horizontal vorticity between the simulations also affect the tilting magnitude, and that aspect will be explored toward the end of the manuscript.

a. *Updraft analysis*

Given the importance of downtilt convective updraft in the generation of negative absolute vorticity, we now examine the causes for differences in the updraft strength in the downtilt convective region by analyzing the vertical momentum budget equation within the downtilt convective updraft column. In the rest of the analysis, for simplicity, we will focus on comparing the CTRL and α40 simulations, which show the largest differences.

For an inviscid fluid, the vertical momentum equation is

$$\frac{\partial w}{\partial t} + \mathbf{u} \cdot \nabla w = -\frac{1}{\rho}\frac{\partial p'}{\partial z} + B, \tag{6}$$

where $\mathbf{u}$ is a three-dimensional wind vector and $p' = p - p_b$ and $B = -g[(\rho - \rho_b)/\rho]$ are the perturbation pressure and buoyancy with respect to basic-state fields of pressure p_b and density ρ_b (defined below). The first term on the right-hand side of (6) is referred to as the vertical perturbation pressure gradient force (VPPGF; Markowski and Richardson 2010; Holton 2004). Smith et al. (2005) discussed the importance of including the radial dependence of the basic-state density and pressure fields in a strongly rotating vortex, such as a TC. The basic, balanced state is represented by thermal wind balance of the background vortex. The buoyancy associated with this background vortex is referred to as the "system buoyancy" in Smith et al. (2005).

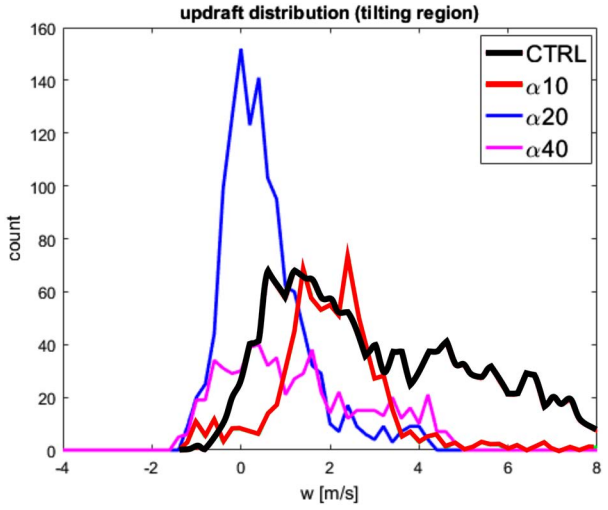

FIG. 13. Histograms of vertical velocity in the downtilt convection where the negative tilting between 8 and 12 km is stronger than -2.5×10^{-3} s^{-1} h^{-1}.

When significant asymmetries are present within a TC, the azimuthal dependence should also be captured (Smith et al. 2005; Zhang et al. 2000; Braun 2002). Given the tilted structure of the TCs in our simulations, the basic state needs to capture both the radial and azimuthal dependences of the system buoyancy. Specifically, Raymond (1992) showed that a tilted balanced vortex has an asymmetric thermal wind structure, with a warm anomaly uptilt and a cold anomaly downtilt. This thermal wind structure can be captured by the balanced state that satisfies both the nonlinear balance equation (NLBE; Charney 1955; Krishnamurti 1968; Haltiner and Williams 1980; Davis and Emanuel 1991; Raymond 1992) and hydrostatic balance. Following this approach, we solve for the three-dimensional balanced pressure p_b and density ρ_b fields, as detailed in appendix B. These balanced fields are then used to define the appropriate VPPGF and buoyancy.

Figure 14 shows the profiles of net upward acceleration and the components of the acceleration supplied by the buoyancy and VPPGF within the downtilt updraft region, averaged between −4 and −2 h before t_w. The CTRL simulation has greater vertical acceleration below 8 km (black solid lines in Fig. 14). Below 2 km, the buoyancy peaks in both the CTRL and α40 simulations. However, larger differences exist in the VPPGF, which are mostly responsible for the CTRL simulation having a larger upward acceleration below 4 km (Fig. 14c). Above 4 km, the buoyancy in the CTRL simulation remains predominately positive due to strong diabatic heating, although it is countered by negative VPPGF above 7 km due to the development of anomalously high pressure at upper levels. In contrast, the buoyancy in the α40 becomes negative above 4 km.

b. *Differences in VPPGF and buoyancy*

Given the differences in VPPGF and buoyancy profiles between the CTRL and α40 simulations, we now examine these components of vertical acceleration in more detail. As shown in Fig. 15, the vertical cross sections through the downtilt convection in the CTRL and α40 simulations (shown in Figs. 12a,d) show that the diabatic heating and vertical mass flux are significantly stronger and deeper in the CTRL simulation, consistent with Figs. 13 and 14. In the CTRL simulation, positive VPPGF (magenta contours) exists in the updraft region below 4 km due to the development of positive perturbation pressure (blue contours) between the main updraft and downdraft at 0–20 km in the cross section. Mass convergence at the edge of the boundary layer low-θ_E region contributes to the positive perturbation pressure (not shown). While similar features exist in the α40 experiment, the main downdraft is located more radially outward and is weaker, and the updrafts are notably weaker and less organized too. As a result, both the positive perturbation pressure and VPPGF are weaker, resulting in a smaller vertical acceleration at low levels in the α40 experiment.

In addition to the stronger lifting due to the VPPGF below 4 km, the downtilt convection in the CTRL simulation also has larger diabatic heat release above 4 km than in the α40 experiment. To examine the cause of this difference, a

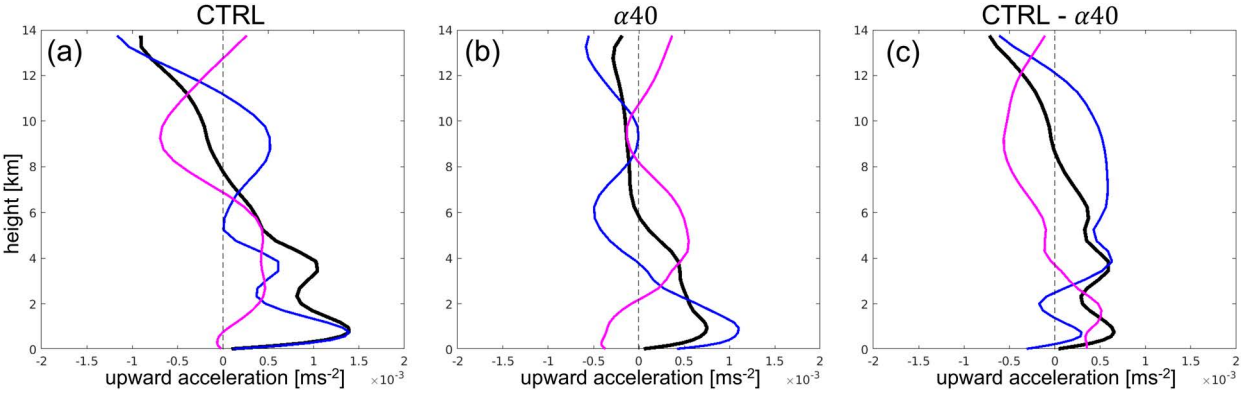

FIG. 14. Profiles of the total upward acceleration (black), VPPGF (magenta), and buoyancy (blue) for the (a) CTRL simulation and (b) α40 simulation in the downtilt updraft region where $w > 0.1$ m s^{-1}, averaged from −4 to −2 h before t_w. (c) The difference between (a) and (b).

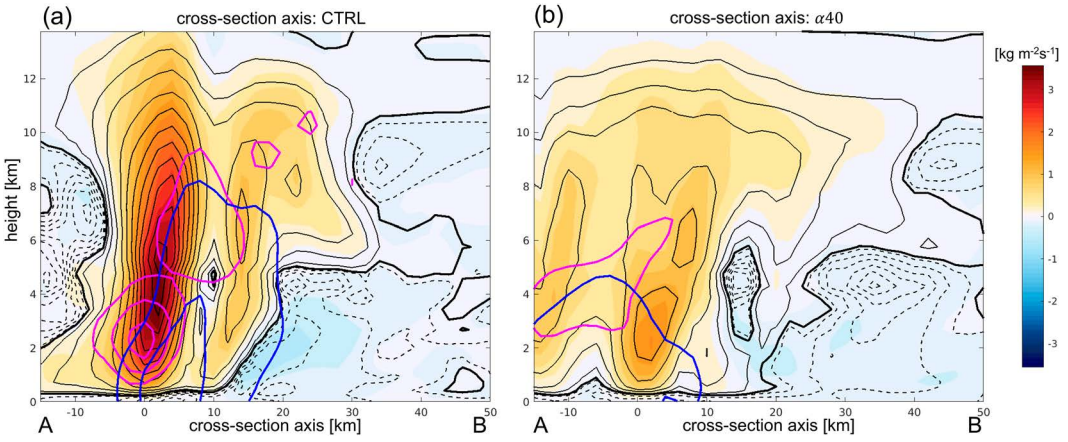

FIG. 15. Cross section of (a) the CTRL simulation and (b) α40 simulation of the vertical mass flux (shaded) and diabatic heating (positive in solid black contours every 0.003 K s^{-1}, and negative in dashed black contours every 0.0003 K s^{-1}), averaged from -4 to -2 h before t_w. Positive, density-weighted VPPGF is shown in the magenta contours every 0.004 kg m^{-2} s^{-2}. Positive pressure perturbation is shown in the blue contours every 22.5 Pa.

Lagrangian back-trajectory analysis is performed at the downtilt convective updraft region of the CTRL and α40 experiments. We seeded initial trajectory locations at grid points between $z = 4$ and 8 km where the difference in vertical velocity between the CTRL and α40 simulations is greater than 0.2 m s^{-1}, as outlined by the magenta contours in Figs. 12a and 12d. Trajectories are integrated backward for 4 h. The total trajectory numbers are 7724 in the CTRL simulation and 8104 in the α40 simulation. To focus on convective air parcels, we isolate the parcels that have a -30 to 0 min average diabatic heating rate greater than two standard deviations from the mean value of all trajectories. Both experiments have similar number of convective parcels (2222 for CTRL and 2227 for α40), which originate from the lower troposphere (Figs. 16).

Comparing the mean θ_E evolution along the convective parcel trajectories (Fig. 17a) shows that the CTRL simulation has slightly larger θ_E than the convective parcel trajectories in the α40 simulation. The standard deviation of θ_E for both simulations is about 3.4 K. To understand this difference in mean θ_E, we compared the trajectory density distribution within the boundary layer. Figure 17b shows that the convective parcels in the CTRL simulation originate over a wider area, with parcels having high-θ_E coming directly from the south. In contrast, the trajectory density in the α40 simulation is more radially confined (Fig. 17c). The left-of-shear low-θ_E region (blue contours), which is associated with rainband downdraft ventilation (Alland et al. 2021a), is located at slightly smaller radii and wraps farther downwind and upshear in the α40 simulation due to the smaller tilt (Figs. 17b,c). Previous studies (e.g., Rios-Berrios et al. 2018) demonstrated that the evolution of vortex tilt and downtilt precipitation is closely linked together, which affects the location of the downward flux of

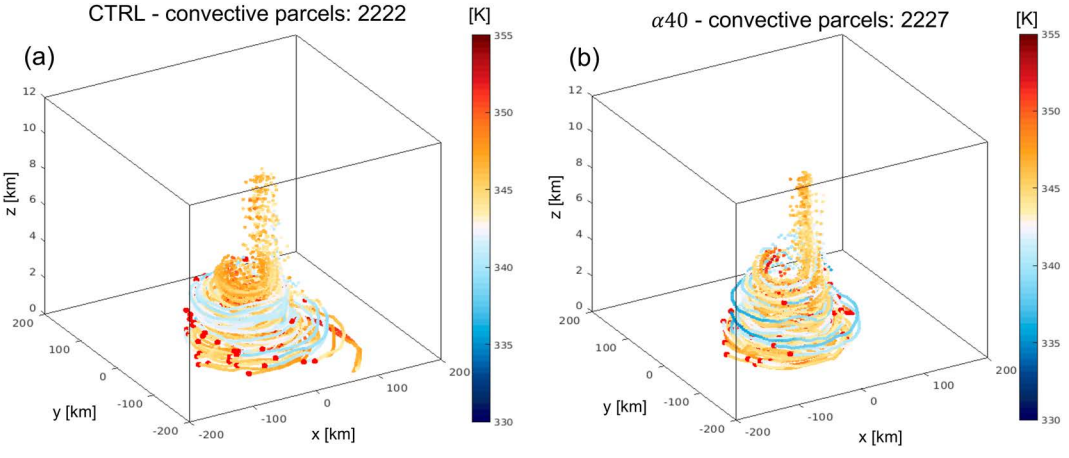

FIG. 16. Four-hour back trajectories of convective air parcels initialized at grid points in the downtilt convective updraft region, as shown in Figs. 12a and 12d, for the (a) CTRL and (b) α40 simulations. Along-trajectory θ_E is colored in dots. The originating locations of the parcel trajectories are colored in red. The number of convective parcels in each experiment is given in each panel title.

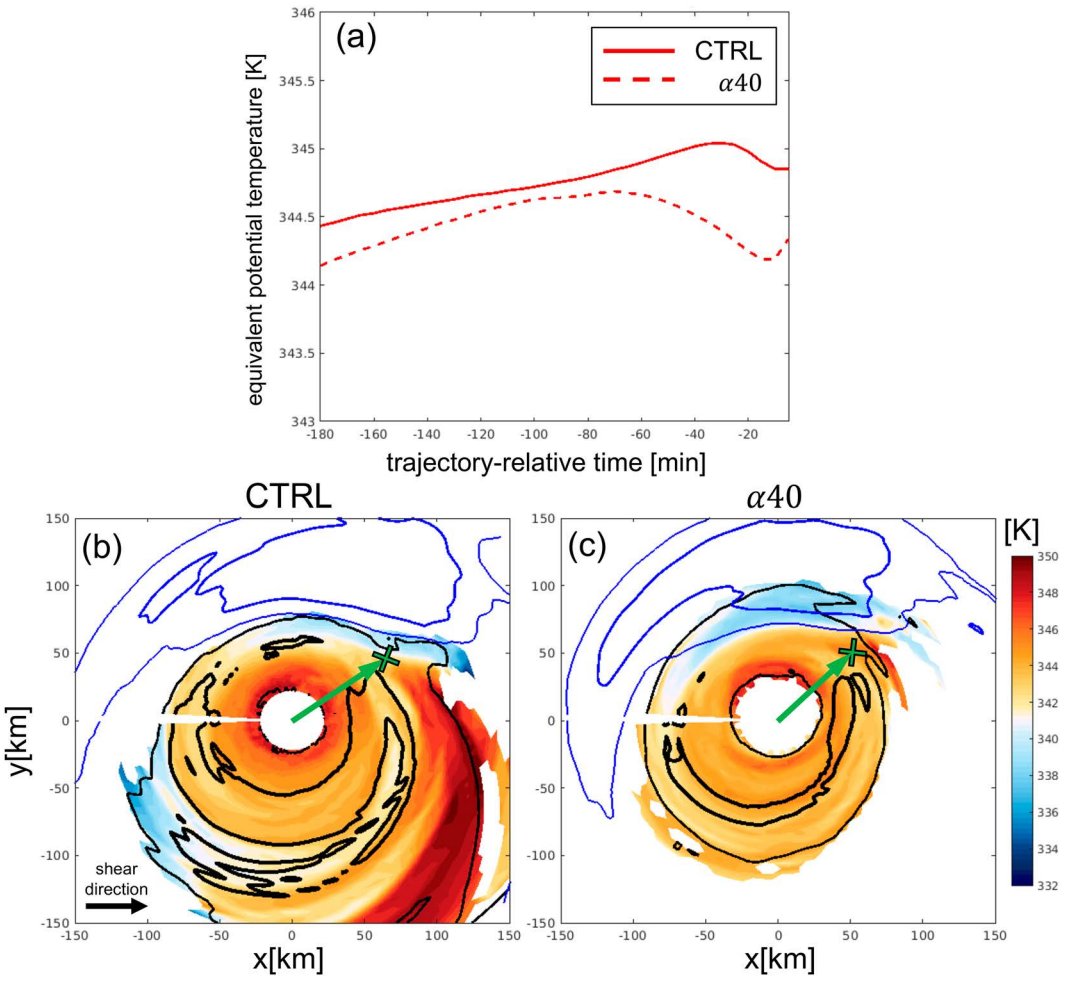

FIG. 17. (a) Mean along-trajectory θ_E of convective air parcels in the CTRL and α40 experiments. (b) Depth-averaged along-trajectory θ_E of the convective parcels in the CTRL experiment. Normalized back-trajectory density below $z = 2$ km over 6 h (normalized by the maximum value; 0.1 thin, black contour and 0.5 thick, black contour). The 0–2-km average θ_E during the same 6-h period is contoured in blue at 337 K (thick contour) and 339 K (thin contour). (c) As in (b), but for the α40 experiment. The black arrow in (b) indicates the shear direction in both experiments. Green arrows and crosses in (b) and (c) indicate the vortex tilt vectors and 6.5-km TC centers.

low-θ_E air entering the boundary layer. Note that this rainband downdraft ventilation, which occurs outside of the radius of maximum wind, is different from the previously described inner-core downdraft ventilation, which is not contained within this subset of back trajectories.

By examining the originating location of the convective parcels (not shown), 8.6% of the convective parcels in the CTRL simulation originate from the left-of-shear, low-θ_E region, in contrast to 15.4% in the α40 simulation. This difference is consistent with the α40 parcel trajectory density having greater overlap with the low-θ_E air of the rainband cold pool compared to the CTRL simulation (Figs. 17b,c). Previous studies showed that boundary layer recovery via surface enthalpy fluxes can negate downdraft ventilation effects (Molinari et al. 2013; Zhang et al. 2013; Chen et al. 2021). Examining the θ_E time series of these parcels originating in the rainband cold pool (not shown) indicates that partial recovery of the θ_E deficit occurs. In the α40 simulation, however, the recovery is limited by the larger number of parcels originating from the left-of-shear, low-θ_E region, despite the larger surface fluxes at smaller radii due to stronger winds. Along with a shorter recovery time scale caused by the farther downwind shift and smaller radial distance of the low-θ_E region, the θ_E of parcels feeding downtilt convection is smaller in the α40 simulation, lowering the eventual buoyancy. In this scenario, these low-θ_E air parcels from rainband downdraft ventilation may counterintuitively be *beneficial* to the longer-term TC intensity, since they prevent a much more disruptive inner-core downdraft ventilation event, which would be more likely to occur if the downtilt convection was stronger and more persistent, as it is in the CTRL simulation.

Additionally, Fig. 17a shows that the convective air parcels in the α40 simulation have a larger drop in mean θ_E by about 0.5 K after −60 min during their ascent. This difference suggests

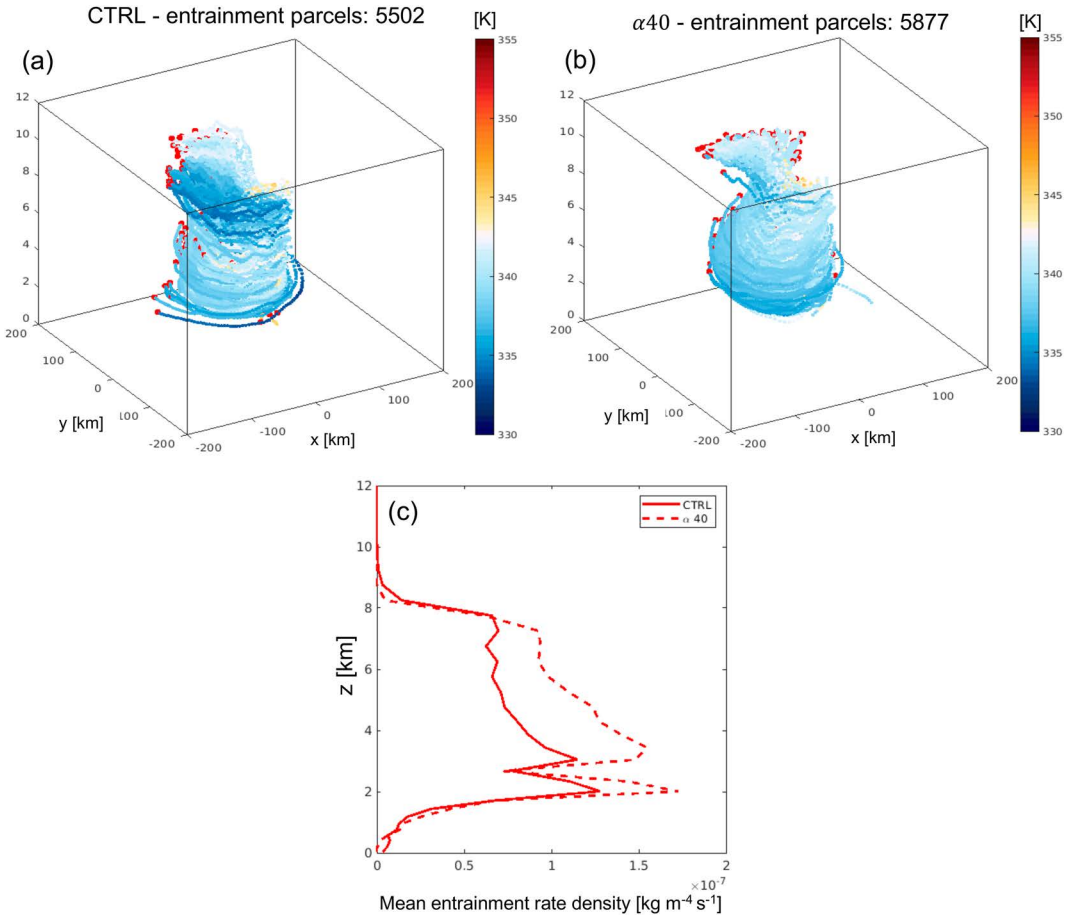

FIG. 18. (a),(b) As in Fig. 16, but for the entrainment parcels. (c) Vertical profiles of the mean entrainment rate density (kg m^{-4} s^{-1}) for the CTRL and α40 experiments averaged from −1 to 0 h of the entrainment parcel trajectories.

that the α40 convective parcels experience stronger entrainment compared to the CTRL parcels, which are more undilute. To quantitatively compare the strength of entrainment between these two experiments, we follow the method proposed by Romps (2010) to compute the entrainment rate at each grid point during the back-trajectory time period. Based on Romps (2010), entrainment (e) and detrainment (d) rates at each grid point can be quantified through the "activity source" function, as defined in Eqs. (18) and (19) of Romps (2010):

$$e = \max\left[0,\ \frac{\partial \rho A}{\partial t} + \nabla \cdot (\rho \mathbf{u} A)\right], \quad \text{and} \tag{7}$$

$$d = \max\left[0,\ -\frac{\partial \rho A}{\partial t} - \nabla \cdot (\rho \mathbf{u} A)\right], \tag{8}$$

where A at a grid point = 1 if the mixing ratio of condensates $q_{\text{cond}} \geq 10^{-5}$ kg kg^{-1} and vertical velocity $w > 0.2$ m s^{-1} and $A = 0$; otherwise, ρ is the dry air density. These thresholds follow those used in Romps (2010). The terms in (7) and (8) are computed using central differencing of 5-min model output. The positive activity source $[(\partial \rho A/\partial t) + \nabla \cdot (\rho \mathbf{u} A)]$ measures the entrainment rate at a grid point. The activity source is then tracked along the trajectories.

Starting from the same back trajectories seeded in the downtilt convective updraft region, a parcel is tagged as an "entrainment parcel" if the averaged activity source along the trajectory from $t = -1$ to 0 h is positive. We impose an additional filtering criterion based on θ_E change of the parcels. For each trajectory, we define $\theta_{E,\text{start}}$ as the average θ_E during $t = -4$ to -2 h. We define $\theta_{E,\text{destination}}$ as the θ_E at $t = 0$ h within the convective updraft region. To ensure that the entrainment parcels contribute to the dilution of θ_E in the downtilt updraft region, we only include entrainment parcels that have $(\theta_{E,\text{destination}} - \theta_{E,\text{start}}) > 0.5$ K, i.e., increase their θ_E due to mixing with greater θ_E air rising in convection. The average $\theta_{E,\text{start}}$ of the entrainment parcels is 339.2 K for both the CTRL and α40 simulations, which is about 5 K lower than the θ_E within downtilt convection.

In both experiments, the entrainment parcels circulate cyclonically from downtilt (northeast) to uptilt (southwest), and descend, as shown in Figs. 18a and 18b. This vertical velocity pattern is consistent with the adiabatic descent associated with the slanted isentropes of a tilted, balanced vortex (Jones 1995; Chen et al. 2006; Boehm and Bell 2021).

Comparing the entrainment rate between the CTRL and α40 experiments, the mean entrainment rate among the

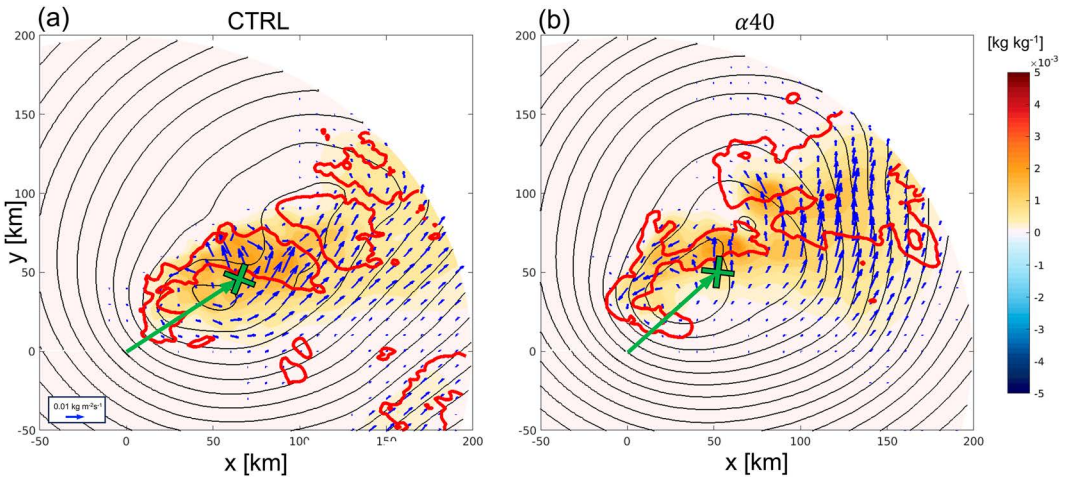

FIG. 19. The 5–9-km averaged snow mixing ratio (shading), streamfunction (black), horizontal mass flux of snow (blue arrows), and flux convergence (red contour at -5×10^{-8} s^{-1}) for (a) the CTRL simulation and (b) the α40 simulation from $t = -4$ to -2 h before t_w. Only the downshear-left quadrant is shown. Green arrows and crosses indicate the vortex tilt vectors and 6.5-km TC centers.

entrainment parcels from -1 to 0 h of the α40 experiment is 2.59×10^{-4} kg m^{-3} s^{-1}, which is about 36% greater than in the CTRL experiment (1.90×10^{-4} kg m^{-3} s^{-1}). To examine the vertical structure of the entrainment, we horizontally integrated the positive activity source over all entrainment parcels from -1 to 0 h. Figure 18c shows a vertical profile of the mean entrainment rate density. The entrainment rate density here measures the amount of mass flux per meter (in kg m^{-4} s^{-1}) entering the downtilt convective region. The α40 simulation has a significantly larger entrainment rate between 3 and 8 km than the CTRL simulation.

c. *Connection to upper-level vortex structure*

How do the vortex tilt and structure influence the diabatic cooling and downdraft structure, as well as the θ_E of the uptilt entraining air parcels? Figure 19 shows that the stronger mid- to upper-level circulation in the α40 experiment, compared to the CTRL, is associated with a larger horizontal flux of snow that transports snow cyclonically downwind and causes the snow flux convergence to occur farther downwind from the convective updraft region. This cyclonic downwind transport of snow leads to a greater separation between the cooling-induced surface cold pool and the high-θ_E region at the downtilt-left quadrant, thus reducing the dynamical lifting at the leading edge of the low-θ_E air in the α40 simulation (Fig. 15b).

Furthermore, the horizontal snow flux in the CTRL simulation predominately points downtilt (Fig. 19a). Together with the slightly larger vortex tilt, the boundary layer low-θ_E region is displaced more radially outward and clockwise compared to the α40 low-θ_E region (Figs. 17b,c). As a result, the low-θ_E air in the CTRL simulation has longer orbiting trajectories and does not negatively affect the downtilt convection.

In addition to the influence on the diabatic cooling and downdraft structure, the stronger upper-level vortex in the α40 simulation also affects the uptilt and inner-core thermodynamic properties. As shown in Figs. 20a and 20b, both the CTRL and α40 simulations have low-θ_E uptilt. Comparing the two experiments shows that the uptilt lower θ_E in the α40 experiment is deeper and colder (magenta contours in Fig. 20b) due to stronger uptilt adiabatic descent (symbolized by the red arrow in Fig. 20d).

To examine the connection between the uptilt descent and vortex structure, Fig. 20d shows that despite the smaller vortex tilt, the tilted vortex in α40 has a stronger inner-core vertical shear associated with the stronger differential tangential wind field and circulation aloft, compared to that in the CTRL simulation (Fig. 20c). Meanwhile, the uptilt warm θ anomaly in the α40 simulation is deeper and stronger between 3- and 6-km altitude compared to that in the CTRL simulation, resulting in a stronger horizontal temperature gradient (Figs. 20c,d) in balance with the stronger vertical shear via thermal wind balance (Raymond 1992; Jones 1995). Previous studies showed that the uptilt adiabatic descent brings midtropospheric dry air downward and, in combination with the stabilization, suppresses convection uptilt (Jones 1995; Chen et al. 2006; Boehm and Bell 2021). The findings of the back-trajectory analysis further show that as the uptilt, low-θ_E air travels cyclonically to the downtilt quadrants, it also entrains into the core region of the downtilt convection at midlevels, reducing diabatic heating and weakening convection.

In addition to the stronger dry air entrainment in the downtilt convection region in the α40 simulation, Fig. 20b shows that upper-level, inner-core θ_E in the α40 simulation is also larger than that in the CTRL simulation, indicating that the upper-level high-θ_E inner core in the α40 simulation is more protected from dry environmental air. This result is consistent with previous studies that showed that a TC vortex with a stronger upper-level vortex circulation is more resilient to VWS (Jones 1995; Riemer and Montgomery 2011; Reasor and Eastin 2012; DesRosiers et al. 2023) and can protect the upper-level inner core from horizontal ventilation, which is

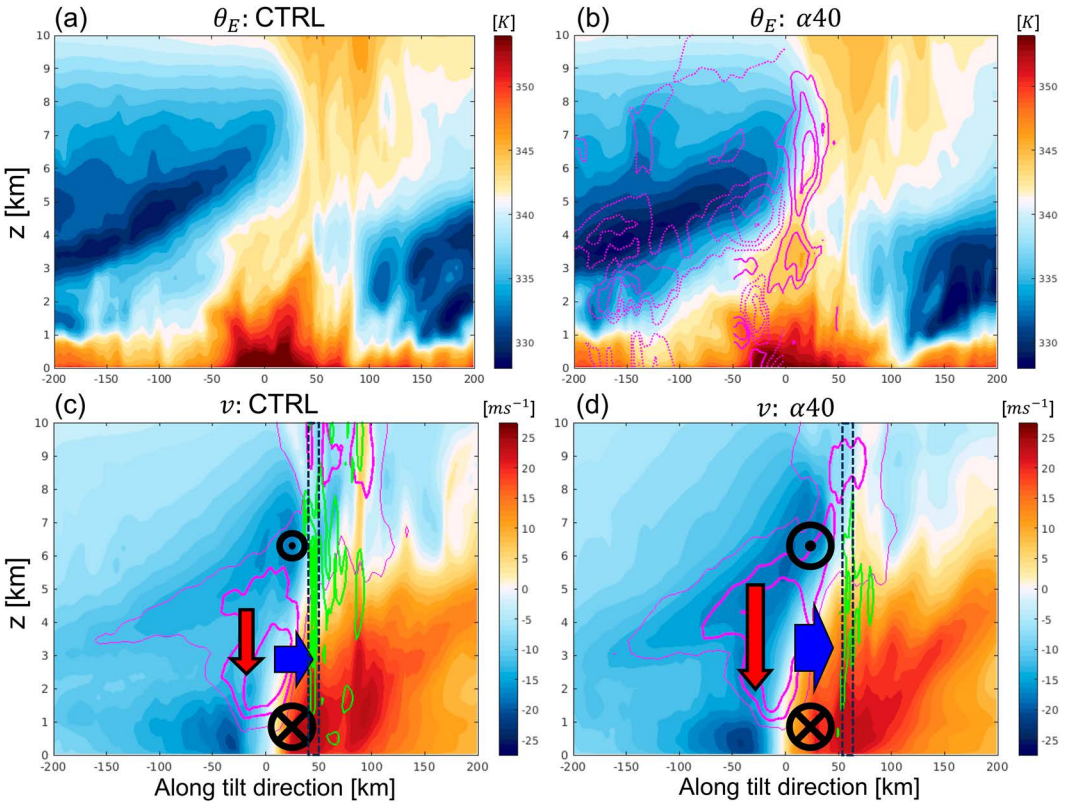

FIG. 20. Along-tilt cross section of the θ_E averaged from $t = -4$ to -3 h before t_w for (a) the CTRL simulation and (b) the α40 simulation. In (b), negative differences in θ_E (α40 − CTRL) uptilt are contoured (dotted magenta lines every 1.2 K from −4.2 to −0.6 K) and positive differences in θ_E from −50 to 50 km are contoured every 1.2 K from 0.6 to 4.2 K. (c),(d) The tangential wind (shaded). The cross (into the page) and dot (out of the page) symbols illustrate the direction and magnitude of the tangential circulation at lower and upper levels to highlight the shear differences between the tilted vortices. Positive potential temperature anomalies are contoured in magenta at every 1.5 K, with the 3 and 4.5 K contours thickened. Red arrows illustrate the uptilt adiabatic descent differences that cause the warm anomaly differences, and blue horizontal arrows represent the strength of the horizontal temperature gradient (pointing from warm to cold). Negative tilting is contoured in green at (−0.5, −2, −3.5, and −5) × 10^{-6} s^{-2}. Black-dashed boxes in (c) and (d) indicate regions where the tilting is most negative.

detrimental to TC intensity (Tang and Emanuel 2010; Riemer and Montgomery 2011; Alland et al. 2021b; Fischer et al. 2023).

Our results presented herein further suggest that the impacts of dry air on the TC intensity have a dependency on the location of the dry-air intrusion and what part of the TC it affects. In the α40 simulation, the stronger upper-level circulation protects the upper-level high-θ_E inner core by reducing inner-core ventilation, while dry air is transported and entrained into the downtilt convection distant from the TC inner core, weakening this downtilt convection. Both of these effects help with the TC organization, allowing cyclonic precession to proceed toward realignment and preventing a much more disruptive inner-core downdraft ventilation event.

Besides the aforementioned mechanisms that impact the downtilt updraft magnitude, the strength of the upper-level vortex also controls the magnitude of horizontal vorticity over the downtilt region *outside* the radius of maximum wind that can be tilted into negative vertical vorticity. To measure the amount of $\boldsymbol{\zeta}_h$ that can be tilted by the horizontal gradient of w, we normalize the tilting term by $|\nabla_h w|$, i.e., $\boldsymbol{\zeta}_h \cdot (\nabla_h w/|\nabla_h w|)$. Figure 21 shows the profiles of normalized tilting, radially averaged over the boxed regions in Figs. 20c and 20d where tilting within the column is most negative. The normalized tilting in the CTRL simulation is about twice as strong as that of the α40 simulation through the column, indicating that the greater available horizontal vorticity below $z = 8$ km contributes to the stronger negative tilting, in addition to the stronger updraft (via $\nabla_h w$). As shown in Fig. 20c, near 50–60 km downtilt, the tangential wind in the CTRL simulation changes from cyclonic to anticyclonic around $z = 5$ km, resulting in horizontal vorticity pointing downtilt. In contrast, the vertical decay of cyclonic tangential wind between $z = 3$ and 7 km and near 50–60 km downtilt is not as rapid in the α40 simulation due to the greater positive vorticity aloft (Fig. 20d). This result suggests that greater vertical vorticity aloft reduces the anticyclonic shear and horizontal vorticity at the downtilt outer core and thus is less conducive for the development of the upper-level negative vorticity region caused by strong downtilt convection.

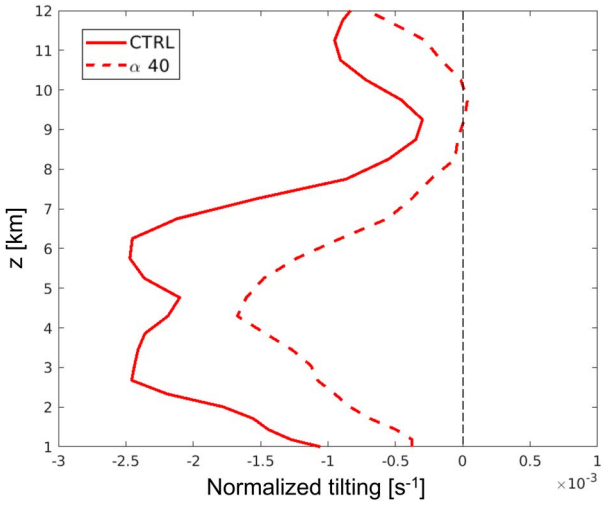

FIG. 21. Vertical profiles of the normalized tilting for the CTRL and α40 experiments from $t = -4$ to -3 h before t_w, averaged over the boxed regions shown in Figs. 20c and 20d.

7. Conclusions

In this study, we examined the processes leading to the divergent outcomes of a set of TC simulations in vertical wind shear of a critical magnitude, which was 7.5 m s^{-1} for our model configuration. A balanced perturbation method was used to enhance the mid- to upper-level, inner-core vorticity of the TCs by various percentages (denoted as α) relative to our unperturbed (CTRL) experiment. This study focused on the divergent intensity and structural evolutions after the precession hiatus (Yu et al. 2023). Without the upper-level vorticity enhancement (CTRL simulation), the TC is unable to resume its cyclonic precession, and it fails to reintensify. On the other hand, the α simulations have less weakening, and the TCs gradually resume their cyclonic precession, becoming more vertically aligned, and reintensify.

The weakening in all the simulations is caused by inner-core ventilation, an inward and downward intrusion of low-θ_E air. The ventilation is strongest in the CTRL simulation and decreases as α increases. A backward trajectory analysis of this low-θ_E air in the CTRL simulation shows that the inward intruding low-θ_E air originates from 6- to 10-km height. Prior to this low-θ_E intrusion, a coherent region of upper-level negative absolute vorticity forms, which is coincident with southern extent of the trajectories. In contrast, the regions of negative absolute vorticity in the α experiments have a weaker magnitude and are less organized. Dynamical analysis based on angular momentum conservation, used to define an "optimal" point given the set of trajectories, shows that this negative absolute vorticity region in the CTRL simulation is inertially unstable, which facilitates the inward acceleration of the environmental, low-θ_E air and strong ventilation of TC inner core. The α simulations, having more positive upper-level vorticity and larger inertial stability aloft, are less conducive for the development of this inward advection of low-θ_E air that feeds the inner-core downdraft ventilation.

A Lagrangian vorticity budget shows that tilting of horizontal vorticity plays an important role in generating the negative absolute vorticity. Subsequently, the negative absolute vorticity is concentrated and enhanced by stretching. The weaker and more disorganized downtilt convective updrafts in the α experiments reduce the tilting magnitude and result in more disorganized areas of negative vorticity. An additional effect is there is less available horizontal vorticity downtilt to be tilted due to the greater positive vorticity aloft and reduced anticyclonic shear. Subsequently, the stretching is also reduced due to weaker vertical divergence between the upper-level updraft and lower-level downdraft. The combination of these effects lessens the development of an inertially unstable region and reduces the low-θ_E intrusion, allowing the TC to recover more quickly for larger α.

Leading up to the inner-core downdraft, a key difference that emerges between the simulations is the strength of persistent, deep downtilt convection. Figure 22 summarizes the various pathways through which a TC with stronger mid- to upper-level vorticity can influence the downtilt convection strength. Comparing the components of the vertical acceleration in the CTRL and α40 simulations, within the downtilt convective

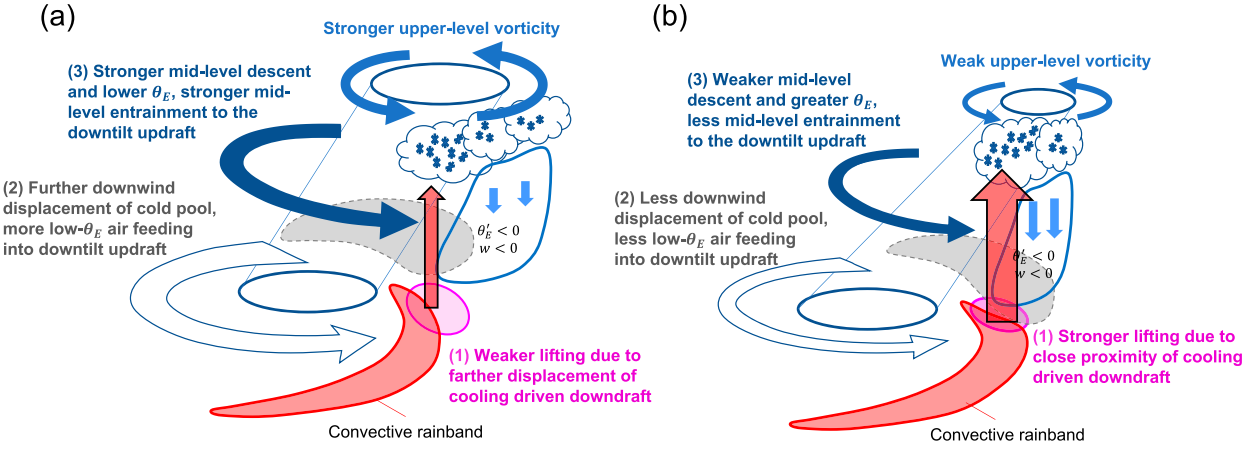

FIG. 22. A schematic diagram summarizing pathways (labeled 1–3) by which the strength of the upper-level circulation influences the downtilt convection strength: (a) a stronger upper-level vortex and (b) a weaker upper-level vortex.

region, there is larger vertical perturbation pressure gradient force (VPPGF) below 4-km height and larger buoyancy above 4 km in the CTRL simulation. This larger VPPGF is due to a positive pressure anomaly located at the convergence of high-θ_E air, circulating in from the downshear right, and low-θ_E air, associated with the downdraft cold pool, as shown in factor 1 of Fig. 22. The stronger upper-level circulation in the α40 simulation advects hydrometeors, produced in the convective updraft, farther cyclonically downwind from the updraft region. As a result, there is larger separation between the cooling-driven downdraft from the convective updraft, resulting in a weaker VPPGF within the downtilt updraft column.

The farther downwind advection of hydrometeors in the α40 simulation also results in more cyclonic downwind displacement of the low-θ_E region left of tilt. As a result, parcels in the α40 simulation that eventually feed the downtilt convection are sourced more from the low-θ_E region, compared to the parcels feeding convection in the CTRL simulation. There is also less time for these low-θ_E parcels to recover before circulating downtilt. Thus, the α40 simulation has lower boundary layer θ_E feeding the downtilt convective updraft region (factor 2 in Fig. 22).

Last, there is deeper and stronger midlevel adiabatic descent uptilt in the α40 simulation compared to the CTRL simulation. In addition to causing a deeper warm and dry anomaly uptilt, lower θ_E air enters the downtilt convective region, resulting in greater entrainment, less diabatic heating, and reduced midlevel buoyancy (factor 3 in Fig. 22).

The pathways summarized above demonstrate the complexity of the intertwined dynamical and thermodynamical processes, modulated by the strength of the mid- to upper-level vorticity (and hence vortex resiliency to VWS). These processes can influence the downtilt convection strength, which is tied to the subsequent inner-core downdraft ventilation event and diverging evolutions of the simulations. These findings may explain why some TCs that display a "central cold cover," similar to the convective character of the CTRL simulation, have slowed or arrested development (Lander 1999). The results also indicate that an accurate representation of the mid- to upper-level vortex structure may be critical for simulating TC intensity and structural evolutions near the critical shear regime in numerical weather prediction models.

In addition, our results show that the upper-level high-θ_E inner core is better protected when the upper-level circulation is stronger, which aligns with previous studies that argued the importance of the TC vertical structure to vortex resiliency in shear (Jones 1995; Riemer and Montgomery 2011; Reasor and Eastin 2012; DesRosiers et al. 2023). Our results further suggest that the impacts of dry air on the TC intensity have a dependency on the location of the dry air intrusion and what part of the TC it affects. A stronger upper-level circulation and less tilted vortex can shield the inner core from dry air (Tang and Emanuel 2010; Riemer and Montgomery 2011), while simultaneously transporting more dry air into the downtilt convection, weakening it. Both of these effects aid the TC in realigning and reintensifying more quickly.

We note that the divergent intensity and structural evolutions explored herein occur at a critical shear regime specific to our simulation design, which may vary depending on various factors, such as environmental and inner-core moisture distribution, shear profile, TC stage, and SST, as well as choices of parameterization schemes. Other caveats should also be noted. For instance, the midlevel vortex in the α experiments is artificially enhanced while keeping the environmental humidity unchanged, while in reality, downtilt convective processes are likely to change the mid- to upper-level vortex strength and the local environmental humidity simultaneously. Given the sensitivities of TC intensity and structural evolutions in this critical shear regime, identifying how this critical shear regime varies as a function of these parameters and parameterization schemes would also be of value.

Acknowledgments. We thank Kristen Corbosiero and three anonymous reviewers for their thoughtful comments on this study. This research was supported by the Office of Naval Research Grants N000142012071 and N000142312443.

Data availability statement. The CM1 namelist files and model output are available upon request via a University at Albany Thematic Real-time Environmental Distributed Data Services (THREDDS) server.

APPENDIX A

Optimal Center Based on Absolute Angular Momentum Conservation

In this appendix, we document the procedure of finding the optimal center with respect to which the absolute angular momentum will be maximally conserved along a given set of trajectories.

Given a set of Lagrangian trajectories, assuming inviscid flow and negligible storm-motion-induced effects, the trajectory-averaged absolute angular momentum budget with respect to a specific center is

$$\left\langle \frac{dM}{dt} \right\rangle = -\left\langle \frac{1}{\rho}\frac{\partial p}{\partial \lambda} \right\rangle, \tag{A1}$$

where $M = rv + (1/2)fr^2$ is the absolute angular momentum, with f being the Coriolis parameter; r and λ are the radius and azimuthal angle for the specific choice of center; and $\langle\rangle$ denotes averaging over the set of trajectories. Note that the definitions of M, r, and azimuthal derivative $\partial/\partial\lambda$ all depend on the choice of center, affecting the conservation. For an axisymmetric vortex, the natural choice of center is the location of minimum pressure, for which the azimuthal gradient of pressure $\partial p/\partial\lambda$ vanishes, and thus, M is conserved. However, for a tilted vortex, the choice of center becomes nontrivial, as the asymmetries in the pressure field result in a nonnegligible pressure gradient torque and M is not conserved.[A1] Despite

[A1] It should be noted that while the pressure gradient torque has nearly zero impact on the conservation of azimuthally averaged M, it redistributes M from one sector of the TC to another and thus can affect the conservation of M along individual trajectories or over a sector of the TC.

this challenge, for a given set of trajectories, it may be possible to define an "optimal" center where the angular momentum defined with respect to this center would be maximally conserved along the trajectories over a certain time period. In other words, the pressure gradient torque with respect to the optimal center is minimized along the trajectories. Based on this objective, the optimal center can be obtained by minimizing the following cost function $J(\mathbf{r}_o)$:

$$J(\mathbf{r}_o) = \sum_t \sum_i \left| -\frac{1}{\rho(\mathbf{x}_i, t)} \frac{\partial p(\mathbf{x}_i, t)}{\partial \lambda} \right|^2 = \sum_t \sum_x \sigma(\mathbf{x}, t) \left| -\frac{1}{\rho(\mathbf{x}, t)} \frac{\partial p(\mathbf{x}, t)}{\partial \lambda} \right|^2 \Delta x \Delta y, \tag{A2}$$

where $\mathbf{r}_o$ is the position vector with respect to the center, t is the time within the trajectory period, λ is the azimuthal angle of the polar coordinate system for a given $\mathbf{r}_o$, i represents an individual trajectory, $\mathbf{x}_i$ is the position vector of each individual trajectory, $\sigma(\mathbf{x}, t)$ is the trajectory density at $\mathbf{x}$ and t, and Δx and Δy are the grid spacing, which are both 2 km here. The second equality of (A2) uses the fact that summing the square of the pressure gradient torque over all trajectories is equivalent to summing the trajectory-density-weighted pressure gradient torque over space. In other words, the cost function prioritizes minimizing the pressure gradient torque over the regions where the trajectory distribution is dense.

For our analysis in section 4a, since the majority of the trajectories descend from levels above 6 km (Fig. 7b), we will focus our analysis during the time period when the mean trajectory height is above 5.5 km. To remove transient, noisy features in pressure gradient torque, a 3-h running average of the pressure gradient torque is used.

APPENDIX B

Balanced Reference State

In this appendix, we document the details of solving for the basic state fields of pressure p_b and density ρ_b associated with a tilted balanced vortex. In CM1, the pressure p is represented through the Exner function $\pi = (p/p_{00})^{R_d/c_p}$, with $p_{00} = 1000$ hPa, and the density is represented through the density potential temperature $\theta_\rho = p/(R\rho\pi)$, where $R = 287.04$ J kg^{-1} K^{-1} is the gas constant for dry air. The thermal wind structure of a tilted vortex can be captured by the balanced states of π_b and $\theta_{\rho b}$ that satisfy both the nonlinear balance equation (NLBE) and the hydrostatic balance. For CM1, these two balances can be written as

$$\nabla_h \cdot (c_p \theta_{\rho b} \nabla_h \pi_b) = 2\left[\frac{\partial^2\psi}{\partial x^2}\frac{\partial^2\psi}{\partial y^2} - \left(\frac{\partial^2\psi}{\partial x \partial y}\right)^2\right] + f\nabla_h^2\psi, \tag{B1}$$

$$c_p \theta_{\rho b} \frac{\partial \pi_b - \pi_0}{\partial z} = g\frac{\theta_{\rho b} - \theta_{\rho 0}}{\theta_{\rho 0}}, \tag{B2}$$

where ψ is the streamfunction of the nondivergent wind of the tilted vortex and $\theta_{\rho 0}(z)$ and $\pi_0(z)$ are prescribed reference state profiles of θ_ρ and π specified by the environmental sounding, respectively. To obtain an appropriate streamfunction that represents the tilted balanced vortex, the vertical relative vorticity ζ is temporally averaged over the analysis time window (denoted as $\overline{\zeta}$), i.e., $t = -4$ to -2 h. The streamfunction ψ at each level is then obtained by solving $\nabla_h^2\psi = \overline{\zeta}$. Note that Eqs. (B1) and (B2) form an equation system for π_b and $\theta_{\rho b}$. In each iteration, π_b is solved using (B1) with zero Dirichlet boundary conditions on the lateral boundaries, which is then followed by an update of $\theta_{\rho b}$ using (B2). This iterative procedure is repeated until convergence is achieved. In general, convergence occurs with about 10–15 iterations, but 30 iterations are used to guarantee convergence.

After π_b and $\theta_{\rho b}$ are obtained, the balanced pressure p_b is computed as

$$p_b = p_{00}\,\pi_b^{c_p/R_d}. \tag{B3}$$

The balanced total density can be computed as

$$\rho_b = \frac{p_b}{R\theta_{\rho b}\pi_b}. \tag{B4}$$

In this solving process, hydrometeors are assumed to be present and are unmodified.

REFERENCES

Alland, J. J., and C. A. Davis, 2022: Effects of surface fluxes on ventilation pathways and the intensification of Hurricane Michael (2018). *J. Atmos. Sci.*, **79**, 1211–1229, https://doi.org/10.1175/JAS-D-21-0166.1.

——, B. H. Tang, K. L. Corbosiero, and G. H. Bryan, 2021a: Combined effects of midlevel dry air and vertical wind shear on tropical cyclone development. Part I: Downdraft ventilation. *J. Atmos. Sci.*, **78**, 763–782, https://doi.org/10.1175/JAS-D-20-0054.1.

——, ——, ——, and ——, 2021b: Combined effects of midlevel dry air and vertical wind shear on tropical cyclone development. Part II: Radial ventilation. *J. Atmos. Sci.*, **78**, 783–796, https://doi.org/10.1175/JAS-D-20-0055.1.

Alvey, G. R., III, E. Zipser, and J. Zawislak, 2020: How does Hurricane Edouard (2014) evolve toward symmetry before rapid intensification? A high-resolution ensemble study. *J. Atmos. Sci.*, **77**, 1329–1351, https://doi.org/10.1175/JAS-D-18-0355.1.

Bhatia, K. T., and D. S. Nolan, 2013: Relating the skill of tropical cyclone intensity forecasts to the synoptic environment. *Wea. Forecasting*, **28**, 961–980, https://doi.org/10.1175/WAF-D-12-00110.1.

Boehm, A. M., and M. M. Bell, 2021: Retrieved thermodynamic structure of Hurricane Rita (2005) from airborne multi–Doppler radar data. *J. Atmos. Sci.*, **78**, 1583–1605, https://doi.org/10.1175/JAS-D-20-0195.1.

Braun, S. A., 2002: A cloud-resolving simulation of Hurricane Bob (1991): Storm structure and eyewall buoyancy. *Mon. Wea. Rev.*, **130**, 1573–1591, https://doi.org/10.1175/1520-0493(2002)130<1573:ACRSOH>2.0.CO;2.

Bryan, G. H., and J. M. Fritsch, 2002: A benchmark simulation for moist nonhydrostatic numerical models. *Mon. Wea. Rev.*, **130**,

2917–2928, https://doi.org/10.1175/1520-0493(2002)130<2917:ABSFMN>2.0.CO;2.

Charney, J. G., 1955: The use of primitive equations of motion in numerical prediction. *Tellus*, **7**, 22–26, https://doi.org/10.3402/tellusa.v7i1.8772.

Chen, S. S., J. A. Knaff, and F. D. Marks Jr., 2006: Effects of vertical wind shear and storm motion on tropical cyclone rainfall asymmetries deduced from TRMM. *Mon. Wea. Rev.*, **134**, 3190–3208, https://doi.org/10.1175/MWR3245.1.

Chen, X., Y. Wang, J. Fang, and M. Xue, 2018: A numerical study on rapid intensification of Typhoon Vicente (2012) in the South China Sea. Part II: Roles of inner-core processes. *J. Atmos. Sci.*, **75**, 235–255, https://doi.org/10.1175/JAS-D-17-0129.1.

——, J.-F. Gu, J. A. Zhang, F. D. Marks, R. F. Rogers, and J. J. Cione, 2021: Boundary layer recovery and precipitation symmetrization preceding rapid intensification of tropical cyclones under shear. *J. Atmos. Sci.*, **78**, 1523–1544, https://doi.org/10.1175/JAS-D-20-0252.1.

Corbosiero, K. L., and J. Molinari, 2002: The effects of vertical wind shear on the distribution of convection in tropical cyclones. *Mon. Wea. Rev.*, **130**, 2110–2123, https://doi.org/10.1175/1520-0493(2002)130<2110:TEOVWS>2.0.CO;2.

Davis, C. A., and K. A. Emanuel, 1991: Potential vorticity diagnosis of cyclogenesis. *Mon. Wea. Rev.*, **119**, 1929–1952, https://doi.org/10.1175/1520-0493(1991)119<1929:PVDOC>2.0.CO;2.

DeHart, J. C., R. A. Houze Jr., and R. F. Rogers, 2014: Quadrant distribution of tropical cyclone inner-core kinematics in relation to environmental shear. *J. Atmos. Sci.*, **71**, 2713–2732, https://doi.org/10.1175/JAS-D-13-0298.1.

DeMaria, M., 1996: The effect of vertical shear on tropical cyclone intensity change. *J. Atmos. Sci.*, **53**, 2076–2088, https://doi.org/10.1175/1520-0469(1996)053<2076:TEOVSO>2.0.CO;2.

——, and J. Kaplan, 1994: A Statistical Hurricane Intensity Prediction Scheme (SHIPS) for the Atlantic basin. *Wea. Forecasting*, **9**, 209–220, https://doi.org/10.1175/1520-0434(1994)009<0209:ASHIPS>2.0.CO;2.

——, M. Mainelli, L. K. Shay, J. A. Knaff, and J. Kaplan, 2005: Further improvements to the Statistical Hurricane Intensity Prediction Scheme (SHIPS). *Wea. Forecasting*, **20**, 531–543, https://doi.org/10.1175/WAF862.1.

DesRosiers, A. J., M. M. Bell, P. J. Klotzbach, M. S. Fischer, and P. D. Reasor, 2023: Observed relationships between tropical cyclone vortex height, intensity, and intensification rate. *Geophys. Res. Lett.*, **50**, e2022GL101877, https://doi.org/10.1029/2022GL101877.

Didlake, A. C., Jr., and R. A. Houze Jr., 2009: Convective-scale downdrafts in the principal rainband of Hurricane Katrina (2005). *Mon. Wea. Rev.*, **137**, 3269–3293, https://doi.org/10.1175/2009MWR2827.1.

Finocchio, P. M., and S. J. Majumdar, 2017: The predictability of idealized tropical cyclones in environments with time-varying vertical wind shear. *J. Adv. Model. Earth Syst.*, **9**, 2836–2862, https://doi.org/10.1002/2017MS001168.

Fischer, M. S., P. D. Reasor, B. H. Tang, K. L. Corbosiero, R. D. Torn, and X. Chen, 2023: A tale of two vortex evolutions: Using a high-resolution ensemble to assess the impacts of ventilation on a tropical cyclone rapid intensification event. *Mon. Wea. Rev.*, **151**, 297–320, https://doi.org/10.1175/MWR-D-22-0037.1.

Frank, W. M., and E. A. Ritchie, 1999: Effects of environmental flow upon tropical cyclone structure. *Mon. Wea. Rev.*, **127**, 2044–2061, https://doi.org/10.1175/1520-0493(1999)127<2044:EOEFUT>2.0.CO;2.

——, and ——, 2001: Effects of vertical wind shear on the intensity and structure of numerically simulated hurricanes. *Mon. Wea. Rev.*, **129**, 2249–2269, https://doi.org/10.1175/1520-0493(2001)129<2249:EOVWSO>2.0.CO;2.

Gao, S., S. Zhai, B. Chen, and T. Li, 2017: Water budget and intensity change of tropical cyclones over the western North Pacific. *Mon. Wea. Rev.*, **145**, 3009–3023, https://doi.org/10.1175/MWR-D-17-0033.1.

Haltiner, G. J., and R. T. Williams, 1980: *Numerical Prediction and Dynamic Meteorology*. 2nd ed. Wiley and Sons, 477 pp.

Hence, D. A., and R. A. Houze Jr., 2008: Kinematic structure of convective-scale elements in the rainbands of Hurricanes Katrina and Rita (2005). *J. Geophys. Res.*, **113**, D15108, https://doi.org/10.1029/2007JD009429.

Holton, J. R., 2004: *An Introduction to Dynamic Meteorology*. 4th ed. Academic Press, 529 pp.

Jones, S. C., 1995: The evolution of vortices in vertical shear. I: Initially barotropic vortices. *Quart. J. Roy. Meteor.*, **121**, 821–851, https://doi.org/10.1002/qj.49712152406.

——, 2000: The evolution of vortices in vertical shear. II: Large-scale asymmetries. *Quart. J. Roy. Meteor. Soc.*, **126**, 3137–3159, https://doi.org/10.1002/qj.49712657008.

Krishnamurti, T. N., 1968: A diagnostic balance model for studies of weather systems of low and high latitudes, Rossby number less than 1. *Mon. Wea. Rev.*, **96**, 197–207, https://doi.org/10.1175/1520-0493(1968)096<0197:ADBMFS>2.0.CO;2.

Lander, M. A., 1999: A tropical cyclone with an enormous central cold cover. *Mon. Wea. Rev.*, **127**, 132–136, https://doi.org/10.1175/1520-0493(1999)127<0132:ATCWAE>2.0.CO;2.

Markowski, P., and Y. Richardson, 2010: *Mesoscale Meteorology in Low Latitudes*. Wiley-Blackwell, 432 pp.

Miyamoto, Y., and D. S. Nolan, 2018: Structural changes preceding rapid intensification in tropical cyclones as shown in a large ensemble of idealized simulations. *J. Atmos. Sci.*, **75**, 555–569, https://doi.org/10.1175/JAS-D-17-0177.1.

Molinari, J., J. Frank, and D. Vollaro, 2013: Convective bursts, downdraft cooling, and boundary layer recovery in a sheared tropical storm. *Mon. Wea. Rev.*, **141**, 1048–1060, https://doi.org/10.1175/MWR-D-12-00135.1.

Nguyen, L. T., and J. Molinari, 2015: Simulation of the downshear reformation of a tropical cyclone. *J. Atmos. Sci.*, **72**, 4529–4551, https://doi.org/10.1175/JAS-D-15-0036.1.

——, ——, and D. Thomas, 2014: Evaluation of tropical cyclone center identification methods in numerical models. *Mon. Wea. Rev.*, **142**, 4326–4339, https://doi.org/10.1175/MWR-D-14-00044.1.

Onderlinde, M. J., and D. S. Nolan, 2017: The tropical cyclone response to changing wind shear using the method of time-varying point-downscaling. *J. Adv. Model. Earth Syst.*, **9**, 908–931, https://doi.org/10.1002/2016MS000796.

Ooyama, K., 1966: On the stability of the baroclinic circular vortex: A sufficient criterion for instability. *J. Atmos. Sci.*, **23**, 43–53, https://doi.org/10.1175/1520-0469(1966)023<0043:OTSOTB>2.0.CO;2.

Peng, K., and J. Fang, 2021: Effect of the initial vortex vertical structure on early development of an axisymmetric tropical cyclone. *J. Geophys. Res. Atmos.*, **126**, e2020JD033697, https://doi.org/10.1029/2020JD033697.

Polvani, L. M., 1991: Two-layer geostrophic vortex dynamics. Part 2. Alignment and two-layer V-states. *J. Fluid Mech.*, **225**, 241–270, https://doi.org/10.1017/S0022112091002045.

Powell, M. D., 1990: Boundary layer structure and dynamics in outer hurricane rainbands. Part II: Downdraft modification and

mixed layer recovery. *Mon. Wea. Rev.*, **118**, 918–938, https://doi.org/10.1175/1520-0493(1990)118<0918:BLSADI>2.0.CO;2.

Raymond, D. J., 1992: Nonlinear balance and potential-vorticity thinking at large Rossby number. *Quart. J. Roy. Meteor. Soc.*, **118**, 987–1015, https://doi.org/10.1002/qj.49711850708.

Reasor, P. D., and M. T. Montgomery, 2001: Three-dimensional alignment and corotation of weak, TC-like vortices via linear vortex Rossby waves. *J. Atmos. Sci.*, **58**, 2306–2330, https://doi.org/10.1175/1520-0469(2001)058<2306:TDAACO>2.0.CO;2.

——, and M. D. Eastin, 2012: Rapidly intensifying Hurricane Guillermo (1997). Part II: Resilience in shear. *Mon. Wea. Rev.*, **140**, 425–444, https://doi.org/10.1175/MWR-D-11-00080.1.

——, and M. T. Montgomery, 2015: Evaluation of a heuristic model for tropical cyclone resilience. *J. Atmos. Sci.*, **72**, 1765–1782, https://doi.org/10.1175/JAS-D-14-0318.1.

——, ——, F. D. Marks Jr., and J. F. Gamache, 2000: Low-wavenumber structure and evolution of the hurricane inner core observed by airborne dual-Doppler radar. *Mon. Wea. Rev.*, **128**, 1653–1680, https://doi.org/10.1175/1520-0493(2000)128<1653:LWSAEO>2.0.CO;2.

——, ——, and L. D. Grasso, 2004: A new look at the problem of tropical cyclones in vertical shear flow: Vortex resiliency. *J. Atmos. Sci.*, **61**, 3–22, https://doi.org/10.1175/1520-0469(2004)061<0003:ANLATP>2.0.CO;2.

——, R. Rogers, and S. Lorsolo, 2013: Environmental flow impacts on tropical cyclone structure diagnosed from airborne Doppler radar composites. *Mon. Wea. Rev.*, **141**, 2949–2969, https://doi.org/10.1175/MWR-D-12-00334.1.

Richardson, J. C., R. D. Torn, and B. H. Tang, 2022: An analog comparison between rapidly and slowly intensifying tropical cyclones. *Mon. Wea. Rev.*, **150**, 2139–2156, https://doi.org/10.1175/MWR-D-21-0260.1.

Riemer, M., and M. T. Montgomery, 2011: Simple kinematic models for the environmental interaction of tropical cyclones in vertical wind shear. *Atmos. Chem. Phys.*, **11**, 9395–9414, https://doi.org/10.5194/acp-11-9395-2011.

——, and F. Laliberté, 2015: Secondary circulation of tropical cyclones in vertical wind shear: Lagrangian diagnostic and pathways of environmental interaction. *J. Atmos. Sci.*, **72**, 3517–3536, https://doi.org/10.1175/JAS-D-14-0350.1.

——, M. T. Montgomery, and M. E. Nicholls, 2010: A new paradigm for intensity modification of tropical cyclones: Thermodynamic impact of vertical wind shear on the inflow layer. *Atmos. Chem. Phys.*, **10**, 3163–3188, https://doi.org/10.5194/acp-10-3163-2010.

——, ——, and ——, 2013: Further examination of the thermodynamic modification of the inflow layer of tropical cyclones by vertical wind shear. *Atmos. Chem. Phys.*, **13**, 327–346, https://doi.org/10.5194/acp-13-327-2013.

Rios-Berrios, R., and R. D. Torn, 2017: Climatological analysis of tropical cyclone intensity changes under moderate vertical wind shear. *Mon. Wea. Rev.*, **145**, 1717–1738, https://doi.org/10.1175/MWR-D-16-0350.1.

——, C. A. Davis, and R. D. Torn, 2018: A hypothesis for the intensification of tropical cyclones under moderate vertical wind shear. *J. Atmos. Sci.*, **75**, 4149–4173, https://doi.org/10.1175/JAS-D-18-0070.1.

Romps, D. M., 2010: A direct measure of entrainment. *J. Atmos. Sci.*, **67**, 1908–1927, https://doi.org/10.1175/2010JAS3371.1.

Rotunno, R., and K. A. Emanuel, 1987: An air–sea interaction theory for tropical cyclones. Part II: Evolutionary study using a nonhydrostatic axisymmetric numerical model. *J. Atmos. Sci.*, **44**, 542–561, https://doi.org/10.1175/1520-0469(1987)044<0542:AAITFT>2.0.CO;2.

Ryglicki, D. R., and R. E. Hart, 2015: An investigation of center finding techniques for tropical cyclones in mesoscale models. *J. Appl. Meteor. Climatol.*, **54**, 825–846, https://doi.org/10.1175/JAMC-D-14-0106.1.

Schecter, D. A., 2015: Response of a simulated hurricane to misalignment forcing compared to the predictions of a simple theory. *J. Atmos. Sci.*, **72**, 1235–1260, https://doi.org/10.1175/JAS-D-14-0149.1.

——, 2020: Distinct intensification pathways for a shallow-water vortex subjected to asymmetric "diabatic" forcing. *Dyn. Atmos. Oceans*, **91**, 101156, https://doi.org/10.1016/j.dynatmoce.2020.101156.

——, 2022: Intensification of tilted tropical cyclones over relatively cool and warm oceans in idealized numerical simulations. *J. Atmos. Sci.*, **79**, 485–512, https://doi.org/10.1175/JAS-D-21-0051.1.

——, and M. T. Montgomery, 2004: Damping and pumping of a vortex Rossby wave in a monotonic cyclone: Critical layer stirring versus inertia-buoyancy wave emission. *Phys. Fluids*, **16**, 1334–1348, https://doi.org/10.1063/1.1651485.

——, and K. Menelaou, 2020: Development of a misaligned tropical cyclone. *J. Atmos. Sci.*, **77**, 79–111, https://doi.org/10.1175/JAS-D-19-0074.1.

——, M. T. Montgomery, and P. D. Reasor, 2002: A theory for the vertical alignment of a quasigeostrophic vortex. *J. Atmos. Sci.*, **59**, 150–168, https://doi.org/10.1175/1520-0469(2002)059<0150:ATFTVA>2.0.CO;2.

Smith, R. K., and M. T. Montgomery, 2015: Toward clarity on understanding tropical cyclone intensification. *J. Atmos. Sci.*, **72**, 3020–3031, https://doi.org/10.1175/JAS-D-15-0017.1.

——, ——, and H. Zhu, 2005: Buoyancy in tropical cyclones and other rapidly rotating atmospheric vortices. *Dyn. Atmos. Oceans*, **40**, 189–208, https://doi.org/10.1016/j.dynatmoce.2005.03.003.

Sprenger, M., and H. Wernli, 2015: The LAGRANTO Lagrangian analysis tool—Version 2.0. *Geosci. Model Dev.*, **8**, 2569–2586, https://doi.org/10.5194/gmd-8-2569-2015.

Tang, B., and K. Emanuel, 2010: Midlevel ventilation's constraint on tropical cyclone intensity. *J. Atmos. Sci.*, **67**, 1817–1830, https://doi.org/10.1175/2010JAS3318.1.

——, and ——, 2012a: Sensitivity of tropical cyclone intensity to ventilation in an axisymmetric model. *J. Atmos. Sci.*, **69**, 2394–2413, https://doi.org/10.1175/JAS-D-11-0232.1.

——, and ——, 2012b: A ventilation index for tropical cyclones. *Bull. Amer. Meteor. Soc.*, **93**, 1901–1912, https://doi.org/10.1175/BAMS-D-11-00165.1.

Tao, D., and F. Zhang, 2014: Effect of environmental shear, sea-surface temperature, and ambient moisture on the formation and predictability of tropical cyclones: An ensemble-mean perspective. *J. Adv. Model. Earth Syst.*, **6**, 384–404, https://doi.org/10.1002/2014MS000314.

Wadler, J. B., D. S. Nolan, J. A. Zhang, and L. K. Shay, 2021: Thermodynamic characteristics of downdrafts in tropical cyclones as seen in idealized simulations of different intensities. *J. Atmos. Sci.*, **78**, 3503–3524, https://doi.org/10.1175/JAS-D-21-0006.1.

Wang, Y., and G. J. Holland, 1996: Tropical cyclone motion and evolution in vertical shear. *J. Atmos. Sci.*, **53**, 3313–3332, https://doi.org/10.1175/1520-0469(1996)053<3313:TCMAEI>2.0.CO;2.

Wernli, H., and H. C. Davies, 1997: A Lagrangian-based analysis of extratropical cyclones. I: The method and some applications. *Quart. J. Roy. Meteor. Soc.*, **123**, 467–489, https://doi.org/10.1002/qj.49712353811.

Yu, C.-L., A. C. Didlake Jr., F. Zhang, and R. G. Nystrom, 2021: Asymmetric rainband processes leading to secondary eyewall formation in a model simulation of Hurricane Matthew (2016). *J. Atmos. Sci.*, **78**, 29–49, https://doi.org/10.1175/JAS-D-20-0061.1.

——, B. Tang, and R. G. Fovell, 2023: Tropical cyclone tilt and precession in moderate shear: Precession hiatus in a critical shear regime. *J. Atmos. Sci.*, **80**, 909–932, https://doi.org/10.1175/JAS-D-22-0200.1.

Zhang, D.-L., Y. Liu, and M. K. Yau, 2000: A multiscale numerical study of Hurricane Andrew (1992). Part III: Dynamically induced vertical motion. *Mon. Wea. Rev.*, **128**, 3772–3788, https://doi.org/10.1175/1520-0493(2001)129<3772:AMNSOH>2.0.CO;2.

Zhang, F., and D. Tao, 2013: Effects of vertical wind shear on the predictability of tropical cyclones. *J. Atmos. Sci.*, **70**, 975–983, https://doi.org/10.1175/JAS-D-12-0133.1.

Zhang, J. A., R. F. Rogers, P. D. Reasor, E. W. Uhlhorn, and F. D. Marks, 2013: Asymmetric hurricane boundary layer structure from dropsonde composites in relation to the environmental vertical wind shear. *Mon. Wea. Rev.*, **141**, 3968–3984, https://doi.org/10.1175/MWR-D-12-00335.1.